Internalization of targeted microbubbles by endothelial cells and drug delivery by pores and tunnels

Beekers, Inés; Langeveld, Simone A.G.; Meijlink, Bram; van der Steen, Antonius F.W.; de Jong, Nico; Verweij, Martin D.; Kooiman, Klazina

Check for updates

Internalization of targeted microbubbles by endothelial cells and drug delivery by pores and tunnels

Inés Beekers [a,b,*], Simone A.G. Langeveld [a], Bram Meijlink [a], Antonius F.W. van der Steen [a], Nico de Jong [a,c], Martin D. Verweij [a,c], Klazina Kooiman [a]

[a] *Department of Biomedical Engineering, Thoraxcenter, Erasmus MC University Medical Center Rotterdam, Office Ee2302, P.O. Box 2040, 3000 CA Rotterdam, the Netherlands*
[b] *Department of Health, ORTEC B.V., Houtsingel 5, 2719 EA Zoetermeer, the Netherlands*
[c] *Laboratory of Medical Imaging, Department of Imaging Physics, Delft University of Technology, Building 22, Room D218, Lorentzweg 1, 2628 CJ Delft, the Netherlands*

ARTICLE INFO

ABSTRACT

Ultrasound insonification of microbubbles can locally enhance drug delivery by increasing the cell membrane permeability. To aid development of a safe and effective therapeutic microbubble, more insight into the microbubble-cell interaction is needed. In this *in vitro* study we aimed to investigate the initial 3D morphology of the endothelial cell membrane adjacent to individual microbubbles ($n = 301$), determine whether this morphology was affected upon binding and by the type of ligand on the microbubble, and study its influence on microbubble oscillation and the drug delivery outcome. High-resolution 3D confocal microscopy revealed that targeted microbubbles were internalized by endothelial cells, while this was not the case for non-targeted or IgG1-κ control microbubbles. The extent of internalization was ligand-dependent, since $\alpha_v\beta_3$-targeted microbubbles were significantly more internalized than CD31-targeted microbubbles. Ultra-high-speed imaging (~17 Mfps) in combination with high-resolution confocal microscopy ($n = 246$) showed that microbubble internalization resulted in a damped microbubble oscillation upon ultrasound insonification (2 MHz, 200 kPa peak negative pressure, 10 cycles). Despite damped oscillation, the cell's susceptibility to sonoporation (as indicated by PI uptake) was increased for internalized microbubbles. Monitoring cell membrane integrity ($n = 230$) showed the formation of either a pore, for intracellular delivery, or a tunnel (i.e. transcellular perforation), for transcellular delivery. Internalized microbubbles caused fewer transcellular perforations and smaller pore areas than non-internalized microbubbles. In conclusion, studying microbubble-mediated drug delivery using a state-of-the-art imaging system revealed receptor-mediated microbubble internalization and its effect on microbubble oscillation and resulting membrane perforation by pores and tunnels.

1. Introduction

Endothelial cells lining the blood vessel walls form an excellent barrier against numerous drugs. The endothelial cell itself is rarely the intended target, as drugs often need to extravasate to reach the underlying diseased tissue. Thus, if extravasation can be locally enhanced, lower dosages of drugs can be administered systemically and therefore lower toxicity will be achieved. Phospholipid-coated microbubbles (1–10 μm in diameter) can do just that: upon ultrasound insonification, microbubbles with a gas core start to oscillate resulting in various mechanical and cellular effects [1]. Microbubbles were developed as ultrasound contrast agents and are widely used in the clinic for diagnostic

ultrasound imaging [2]. Drug delivery is enhanced by oscillating microbubbles through different pathways: by perforation of the cell membrane, referred to as sonoporation, by opening intercellular junctions or cell-cell contacts, and by stimulating endocytosis [3–5]. While the exact mechanisms are not fully understood [1,3,5,6], it is clear that there exists a delicate balance between stable microbubble oscillation leading to enhanced drug delivery and more violent microbubble oscillation or inertial cavitation causing irreversible damage [3,7,8]. More insight in the interaction between microbubbles and endothelial cells is needed to facilitate translation to safe and effective clinical use of phospholipid-coated microbubbles for locally enhanced drug delivery.

Previous work on endothelial cells has mostly focused on

establishing the relationship between the microbubbles' acoustic behavior and subsequent cellular effects such as intracellular drug uptake, opening of cell-cell contacts, and intracellular calcium fluctuations [3–6,9–13]. However, the therapeutic outcome in terms of drug delivery enhancement is expected to also depend on the microbubble-cell morphology prior to ultrasound insonification. This morphology may be altered upon phagocytosis or internalization of microbubbles, as has been observed since the first generation of ultrasound contrast agents. Contrast enhanced ultrasound imaging has shown hepatosplenic uptake of microbubbles stabilized by either a polymer shell in Sonovist [14,15], a surfactant in Levovist [16–18], or a phospholipid shell in BR14 [19] and Sonazoid [18,20]. Additionally, a spleen-specific uptake has been shown for SonoVue [21]. The uptake of microbubbles gives a late phase contrast enhancement that is sustained after the typical blood pool phase, because only the microbubbles that are phagocytosed are not washed away in the blood stream and remain to provide contrast for contrast-enhanced ultrasound imaging. The hepatosplenic uptake has been attributed to the phagocytosis by Kupffer cells in particular [18]. Phagocytic ratios differ for various contrast agents, influenced by for instance the charge of the microbubble or the shell composition [18,22,23].

Although macrophages and neutrophils are the classic examples of phagocytic cells, endothelial cells can also internalize particles through phagocytosis. Human umbilical vein endothelial cells (HUVECs) have been shown to phagocytose lipid droplets [24], bacteria [25], and micron-sized magnetic beads conjugated to an VEGFR2 antibody [26]. However, up to now microbubble-cell interaction has been investigated mostly using two-dimensional (2D) imaging and with a focus on what happens after microbubble oscillation, thereby lacking the ability to identify the occurrence of phagocytosis and how it possibly affects microbubble-mediated drug delivery. To incorporate possible phagocytosis into the understanding of sonoporation mechanisms, the microbubble-cell morphology prior to oscillation must be studied in three dimensions (3D). Additionally, 3D imaging is also essential for a holistic view of sonoporation after ultrasound, since Helfield et al. [10] have shown how sonoporation of endothelial cells can be transmembrane in nature.

When studying therapeutic applications, targeted microbubbles have been reported to result in a better therapeutic outcome than non-targeted microbubbles [27]. This inspired the idea that there may be a receptor- or ligand-dependent component influencing the efficacy of enhanced drug delivery by ultrasound-activated microbubbles. A comprehensive study focusing on the microbubble-cell configuration, or morphology of targeting, both prior to and after ultrasound activation, will give valuable insights for future development of targeted microbubbles for therapeutic applications.

The aim of this study was to investigate the 3D morphology of the endothelial cell membrane adjacent to a microbubble and the resulting drug delivery response upon ultrasound insonification. The phagocytosis of microbubbles by endothelial cells was evaluated as internalization, identified by localization of the microbubble between the cell membranes using 3D confocal microscopy for non-targeted, $\alpha_v\beta_3$-targeted, CD31-targeted, and IgG1-κ control microbubbles. Additionally, the oscillatory response of the microbubbles was quantified by ultra-high-speed imaging. The influence of microbubble-cell morphology on the drug delivery potential was evaluated by studying propidium iodide (PI) uptake and membrane perforation upon microbubble oscillation for each microbubble type.

2. Materials and methods

2.1. Microbubble preparation and targeting

The four types phospholipid-coated biotinylated microbubbles (non-targeted, $\alpha_v\beta_3$- and CD31-targeted, and IgG1-κ control) were produced in-house with a C_4F_{10} gas core according to the indirect method as described previously [28,29]. The coating composition included 1,2-distearoyl-sn-glycero-3-phosphocholine (DSPC; 84.8 mol%; Lipoid GmbH, Ludwigshafen, Germany), polyoxyethylene-40-stearate (PEG-40 stearate; 8.2 mol%; Sigma-Aldrich, Zwijndrecht, the Netherlands), 1,2-distearoyl-sn-glycero-3-phosphoethanolamine-N-[carboxy(polyethylene glycol)-2000] (DSPE-PEG(2000); 5.9 mol%; Iris Biotech GmbH, Marktredwitz, Germany), and 1,2-distearoyl-sn-glycero-3-phosphoethanolamine-N-[biotinyl(polyethylene glycol)-2000] (DSPE-PEG(2000)-biotin; 1.1 mol%; Avanti Polar Lipids, Alabaster, Alabama, USA). In short, all components were dissolved in chloroform:methanol (9:1 *v/v*), which was evaporated with argon gas (Linde Gas Benelux, Schiedam, the Netherlands). The lipid film was first freeze-dried (Alpha 1–2 LD plus; Mertin Christ GmbH, Osterode am Harz, Germany), then dispersed in PBS with lipid dye DiD (1,1′-dioctadecyl-3,3,3′,3′-tetramethylindodicarbocyanine perchlorate; Thermo Fisher Scientific, Waltham, MA, USA) to fluorescently label the microbubble coating. The solution was next placed in a sonicator bath for 10 min and then the mixture was further dispersed using low power probe sonication (Sonicator ultrasonic processor XL2020, HeatSystems, Farmingdale, NY, USA) for 5 min. Finally, microbubbles were produced by high power probe sonication for 1 min, under constant flow of C_4F_{10}.

Microbubbles were functionalized to target $\alpha_v\beta_3$ or CD31 using biotin-streptavidin bridging as described previously [12,30]. Previously performed targeting specificity assays using the same CD31 [31], $\alpha_v\beta_3$ [9] and igG1-k [9] antibodies showed the specific binding of CD31- and $\alpha_v\beta_3$-microbubbles to HUVEC. Before targeting, microbubbles were first washed three times by centrifugation at 400*g* for 1 min, then counted with the Coulter Counter Multisizer 3 (50 μm aperture tube, Backman Coulter, Mijdrecht, the Netherlands). Next, 6×10^8 microbubbles were incubated with 60 μg streptavidin (Sigma-Aldrich) for 30 min on ice, washed once, then incubated for 30 min on ice with 6 μg of either biotinylated anti-human CD51/61 antibody (i.e. $\alpha_v\beta_3$; BioLegend, San Diego, CA, USA) or biotinylated anti-human CD31 antibody (R&D Systems, Minneapolis, MN, USA). After incubation one final washing step was performed and the targeted microbubbles were counted to determine the final concentration and size distribution. Control microbubbles were functionalized with IgG1-κ, a biotinylated isotype control antibody for both the CD31 and $\alpha_v\beta_3$ antibody (Sony Biotechnology, San Jose, CA, USA). When using non-targeted microbubbles, these were taken from the counted stock after the first three wash steps.

The average microbubble concentration (standard deviation between brackets) after production was $9.9\ (3.3) \times 10^8$ microbubbles (MB)/ml for non-targeted microbubbles, $3.9\ (0.8) \times 10^8$ MB/ml for $\alpha_v\beta_3$-targeted microbubbles, $2.9\ (1.4) \times 10^8$ MB/ml for CD31-targeted microbubbles, and $2.2\ (0.7) \times 10^8$ MB/ml for igG1-κ control microbubbles. Their average diameter (standard deviation between brackets) was 4.23 (0.29) μm for non-targeted microbubbles, 4.38 (0.10) μm for $\alpha_v\beta_3$-targeted microbubbles, 4.02 (0.32) μm for CD31-targeted microbubbles, and 5.08 (0.27) μm for igG1-κ control microbubbles.

2.2. Endothelial cell culture

All experiments were performed with primary human umbilical vein endothelial cells (HUVECs) from pooled donors (C2519A, LOT 437550, Lonza, Verviers, Belgium) with passage number 4 to 8. The HUVECs were cultured with Endothelial Cell Growth Medium (EGM)-2 (Lonza) in T75 flasks and grown at 37 °C and 5% CO_2 in a humidified incubator to full confluency before replating. Before each experiment, the HUVECs were detached with Accutase solution (Sigma-Aldrich) and replated on the bottom membrane of an acoustically compatible CLINIcell [32] (Mabio, Tourcoing, France) with 50 μm membranes (25 μm²) in 12 ml EGM-2. CLINIcells were incubated for two days at 37 °C and 5% CO_2 to achieve a fully confluent monolayer [9,12]. In total, 23 cultured CLINIcells were used for experiments.

2.3. Experimental set-up

To investigate the microbubble-cell interaction in 3D, a custom-built system consisting of a confocal microscope (Nikon A1R+, Nikon Instruments, Amsterdam, the Netherlands) coupled to the Brandaris 128 ultra-high-speed camera (built in-house [33]) was used as described previously [9,12,34]. In short, a CLINIcell was placed into a water tank at 37 °C for simultaneous imaging and ultrasound insonification (Fig. 1A). At 45° incidence angle, a single element focused transducer (2.25 MHz center frequency; 76.2 mm focal length; − 6 dB beam width at 2 MHz of 3 mm; V305, Panametrics-NDT, Olympus, Waltham, MA, USA) was mounted in the water tank after calibration with a needle hydrophone (1-mm diameter, PA2293, Precision Acoustics, Dorchester, UK). The ultrasound and optical foci were aligned using a pulse-echo approach and a needle tip located at the optical focal plane [35]. Next, the cells were insonified with a single 2 MHz and 10-cycle burst by an arbitrary waveform generator (33220A, Agilent, Palo Alto, CA, USA). A peak negative pressure (PNP) of 200 kPa at the focus was generated with a broadband amplifier (ENI A-500, Electornics & Innovation, Rochester, NY, USA).

2.4. Live cell experimental protocol

The cell membranes were stained with CellMask™ Green Plasma Membrane Stain (Thermo Fisher Scientific) by incubating with 4 μg/ml final concentration for 10 min inside the cell incubator. Next, Hoechst 33342 (5 μg/ml final concentration; Thermo Fisher Scientific) was added to stain the cell nuclei, propidium iodide (PI; 25 μg/ml final concentration; Sigma-Aldrich) was added as a marker for sonoporation, and a final concentration of 1×10^5 microbubbles/ml was added. The CLINIcell was incubated during 5 min in the cell incubator while turned upside down (i.e., with the cells on top). This allowed microbubbles to float towards the cells and, in the case of targeted microbubbles, allow them to bind to the cells. This was done for all types of microbubbles to ensure a proper control experiment in the case of non-targeted and IgG1-κ control microbubbles.

Fig. 1 shows a schematic of the different CLINIcell configurations used for imaging, with either the microbubbles positioned under the cells (Fig. 1B) or the microbubbles positioned above the cells (Fig. 1C). For non-targeted and IgG1-κ microbubbles the configuration with microbubbles above the cells is not experimentally feasible, since the microbubble would float up and away from the cell. From now on we will refer to targeted microbubbles as $\alpha_v\beta_{3\text{-under}}$ and $CD31_{under}$ when positioned under the cells, while $\alpha_v\beta_{3\text{-above}}$ and $CD31_{above}$ will indicate they are positioned above the cells. To image the CLINIcell as depicted in

Fig. 1C, the CLINIcell was turned upright after the last incubation step and the top membrane without cells was cut out from the CLINIcell to enable imaging with an objective with a working distance smaller than the 5 mm spacing between the CLINIcell membranes. A 100× water dipping objective (CFI Plan 100XC W, 2.5 mm working distance, Nikon Instruments, Amsterdam, the Netherlands) was used with four laser channels to image the microbubble-cell interaction: (1) Hoechst excited at 405 nm, detected at 450/50 nm (center wavelength/bandwidth), (2) CellMask Green excited at 488 nm, detected at 525/50 nm, (3) PI excited at 561 nm, detected at 595/50 nm, and (4) DiD excited at 640 nm, detected at 700/75 nm. Channel 1 and 4 were excited and detected simultaneously because there is no spectral overlap between Hoechst and DiD.

To image the microbubble-cell morphology in 3D prior to microbubble oscillation, first a Z-stack was acquired with 0.33 μm steps and at 0.12 μm/pixel (FOV of 256 × 256 pixels). Next, the microbubble oscillation and cellular response upon ultrasound insonification were imaged in 2D at 0.25 μm/pixel (FOV of 256 × 256 pixels), similarly to as described previously [9,12]. In short, a time-lapse of 3 min was acquired with 2.6 frames per second (fps). After approximately 30 s, the light path was automatically switched from the confocal to the Brandaris 128 ultra-high-speed camera to record the microbubble oscillation during ultrasound insonification at ~17 Mfps. The start of ultrasound insonification was defined as $t = 0$ s. Once completed, the light path was automatically switched back to the confocal to monitor the cellular response for at least 2.5 min. After time-lapse imaging was completed, another Z-stack was acquired to observe the cellular effect of microbubble oscillation in 3D.

To obtain a control measurement of the cell thickness without a microbubble, Z-stacks were also taken of FOVs without a microbubble on the cell. To mimic both set-up orientations images were taken of cells when under the CLINIcell membrane (configuration Fig. 1B, 'under') and when above the CLINIcell membrane (configuration Fig. 1C, 'above').

2.5. Chromatic aberration

The 100× water dipping objective used in this study was not corrected for axial chromatic aberration. Therefore, during confocal microscopy different excitation wavelengths were focused onto different planes and lead to a slight displacement of the four imaging wavelengths along the focal axis. In this study, we were especially interested in the axial colocalization of the green 488 nm channel (i.e. the cell membrane) and the far-red 640 nm channel (i.e. the microbubble shell). Therefore, the axial offset between these two channels was quantified by acquiring a confocal microscopy z-stack (21 slices with 0.2 μm step size) of the reflection from a glass coverslip [36]. The focal plane for each channel was obtained by fitting a Gaussian to the intensity profile along the z-axis, similar to the internalized depth image analysis, as explained below. The focal plane of the far-red channel (640 nm) was found to appear 0.32 μm closer to the objective than the green (488 nm) channel. During the quantification of the axial location of the microbubble, we compensated for this axial offset of 0.32 μm.

2.6. Microbubble internalization image analysis

Microbubble internalization by an endothelial cell was quantified using the Cell Mask™ green and DiD channels of the z-stacks before ultrasound by using a custom semi-automated procedure in MATLAB (2019b, The Mathworks Inc., Natick, MA, USA). A step-by-step example of the internalized depth analysis is presented in Supplementary Fig. 1. First of all, to identify the orthogonal planes slicing through the center of the microbubble, in the xy-plane with maximum sum of DiD intensity the microbubble was located (*imfindcircles* function). Next, the xz- and yz-planes intersecting at the center of the microbubble were used to quantify the internalization depth (red lines in Supplementary Fig. 1A).
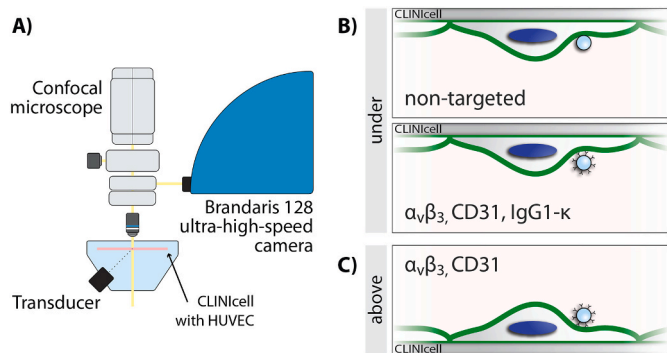
Fig. 1. Schematic representation of the experimental set-up and sample orientations to study microbubble-cell morphology and drug delivery outcome. A) System for simultaneous high-resolution imaging and ultrasound insonification of the CLINIcell with Human Umbilical Vein Endothelial Cells (HUVEC). B) Orientation with microbubbles under the cells. C) Orientation with microbubbles above the cells.

In the DiD channel of the intersection planes (Supplementary Fig. 1B), the upper half of the microbubble (closest to the objective) has the highest fluorescent intensity because only the upper half can be imaged without artefacts due to the gas core. Therefore, a circular fit (*circfit*) through the maximum of each z-intensity profile in both intersection planes was used to identify the microbubble location (red circle in Supplementary Fig. 1B). Next, in the CellMask Green channel of the same intersection planes the apical and basal cell membrane were identified. Since the microbubble's gas core may alter the cell membrane's visualization, the membranes were tracked on the side of the microbubble. For each z-intensity profile, two Gaussian non-linear least square fits (*gauss1*) were used to identify the apical and the basal membrane (Supplementary Fig. 1D). This was repeated for all z-profiles within 4 μm to the left and right of the microbubble. A linear least-squares fit (*poly2*) through the maximum of the Gaussian fit provided the apical and basal cell membranes at the microbubble (Supplementary Fig. 1C). Finally, the internalized depth was quantified as the difference between the z-plane of the apical cell membrane at the microbubble's center and the z-plane of the microbubble closest to the basal membrane (top of microbubble when under the cell and bottom of the microbubble when above the cell). Due to the limited axial resolution (600 nm with the current 100× objective) [37], the distorted imaging through the gas core of a microbubble, and the common inhomogeneities in the cell membrane staining, the determined z-plane of the microbubble did not always intersect with the z-plane of the apical cell membrane or lie inside the cell, resulting in a negative internalization depth. Similarly, the microbubble's z-plane was sometimes deeper than the z-plane of the basal cell membrane, resulting in a relative internalization up 101%.

To quantify how deep a microbubble went into a cell, the cell thickness at the microbubble location was also quantified for all field of views (FOVs) as the difference between the apical and basal cell membranes at the microbubble's center. Since the endothelial cell thickness is known to vary depending on the location on the cell, being thickest around the nucleus and thinning towards the edges, the effect of microbubble location on internalization was also evaluated. The microbubble location on the cell was quantified as the distance from the microbubble to the closest cell edge in the first frame of confocal microscopy time-lapse imaging, as previously described [12].

The occurrence of distinctive cell membrane morphological traits identified in the CellMask Green channel was manually scored for all FOVs with microbubbles. We evaluated for the presence of four different traits at the microbubble location: 1) a circular area of decreased intensity in the xy-plane, referred to as 'shadow' (Supplementary Fig. 2F); 2) a high intensity ring in the xy-plane, referred to as 'green ring' (Supplementary Fig. 2C and D); 3) a protrusion of the cell membrane in the xz- and yz-plane, referred to as 'dome' (Supplementary Fig. 2D); and 4) the presence of green signal around the microbubble shell outside the cell, referred to as 'dye-transfer' (Supplementary Fig. 2F).

2.7. Ultra-high-speed imaging analysis

The microbubble radius upon ultrasound insonification as a function of time was quantified from the Brandaris 128 ultra-high-speed recordings using custom-designed image analysis [38]. Microbubble excursion amplitude was defined as the difference between the maximum radius (R_{max}) and the initial radius (R_0, determined from the first 10 frames without ultrasound). The oscillation amplitude thresholds for sonoporation were determined by linear discriminant analysis, as previously described [12,13].

2.8. Drug delivery image analysis

The cellular response after ultrasound was evaluated for sonoporation, identified as a local increase of PI in the cell on which the microbubble was located. The sonoporated cells were also delineated using custom-built image analysis software to quantify the amount of PI uptake over time, as previously described [9,12]. To quantify membrane perforation, a semi-automated custom-built image analysis script in MATLAB was used to automatically track the perforated area in the CellMask Green channel as a function of time after insonification. In the first confocal microscopy frame after ultrasound an initial square region of interest (ROI) was drawn, approximately 6 × 6 μm. Within this initial ROI, the script searched for a local decrease of CellMask green intensity, defined as a connected region (*bwconncomp*) of more than 3 pixels that have a fluorescent intensity lower than 2/3 of the mean intensity in the ROI (after *imfill* of holes, at 4-pixel connectivity). For each time point, this analysis was repeated in a ROI defined by the bounding box of the previously found perforated area increased by 5 μm in width and height (or the initial square ROI, as long as no perforated area could be identified). Next, a perforated area was classified as a *pore* when there was still CellMask signal remaining or as a *tunnel* when there was no apparent CellMask fluorescent intensity remaining in the perforated area, hence comparable to the background noise level.

To assess the reversibility of sonoporation, the PI uptake time profiles were further analyzed to determine the size and resealing coefficients of the intracellular perforations, as mathematically described by Fan, et al. [39]. The mathematical fit and subsequent classification of cells into categories was done as previously described [9,12,40]. Briefly, the sum of PI fluorescent intensity in the delineated cell, *F(t)*, was fitted to

$$F(t) = \frac{\alpha}{\beta}\left(1 - e^{-\beta t}\right) \tag{1}$$

where *α* is the perforation size coefficient and *β* the perforation resealing coefficient. When *F(t)* did not reach 90% of its asymptotic value within 120 s (i.e. $\beta < -\ln(1 - 0.9)/120\ \text{s}^{-1}$), cells were classified as *non-resealing* and thus irreversibly sonoporated [40]. Next, all PI uptake curves that stabilized within 120 s (i.e. $\beta \geq -\ln(1 - 0.9)/120\ \text{s}^{-1}$) were additionally classified using PCA, resulting into two sub-categories: one with relatively low size and high resealing coefficients, from now on referred to as *resealing* and thus reversibly sonoporated [40], and one with relatively high size and low resealing coefficients, from now on referred to as *saturated*. This last category was classified as *saturated* because these PI uptake profiles typically stabilize due to image saturation or DNA/RNA saturation instead of pore resealing, as previously described [12], and are therefore indicative of severe cell damage upon sonoporation.

2.9. Statistical analysis

Statistical analysis was performed using MATLAB. Data was tested for normality using the Shapiro-Wilk test. For data that was not normally distributed, the Kruskal-Wallis test was performed to evaluate whether groups ($n > 2$) originated from the same distribution. When the Kruskal-Wallis test was rejected at a significance level of $p < 0.05$, follow-up multiple comparison Mann-Whitney tests on pairs with a Bonferroni correction were performed to determine which groups were statistically significantly different. To determine the correlation between non-normally distributed parameters, the Spearman's rank-order correlation was evaluated. Categorical data was tested for significant differences among groups using a Fisher's exact test, accounting for possible zero occurrence.

To explore the influence and correlation of the many different parameters involved in microbubble internalization and microbubble-mediated drug delivery, principal component analysis (PCA) was applied. PCA was used since this method reduces the dimensionality of a large dataset, thereby increasing its interpretability, by computing the principal components (i.e. eigenvectors) along which the data has the largest variance and quantifying how much variance there is in each direction (i.e. the corresponding eigenvalues). The principal components were calculated for the microbubble excursion amplitude,

internalized depth, distance from the microbubble to the nearest cell edge, and cell thickness. This was employed to explore the differences between the microbubble types and set-up orientations and drug delivery outcomes.

All graphical representations using boxplots display the median and interquartile range (IQR), using the standard whiskers ranging from the first quartile minus 1.5 times the IQR up to the third quartile plus 1.5 times the IQR, and show outliers outside this range with black dots.

3. Results

3.1. Microbubble internalization

The position and morphology of a microbubble with respect to a cell was evaluated for 221 FOVs with a microbubble underneath a cell and for 80 FOVs with a microbubble above a cell, with $n \geq 39$ for each microbubble type and orientation. The detailed n numbers for each microbubble type can be found in Supplementary Table 1.

In Fig. 2, typical examples of the 3D microbubble-cell morphology are shown for each microbubble type and set-up orientation. Fig. 2A shows a non-targeted microbubble (diameter (Ø) = 3.5 μm) underneath the cell and without any apparent alteration of the cell membrane (Supplementary Fig. 2A). By quantifying the distance between the

microbubble and the apical membrane, the internalized depth was found to be −0.2 μm. Fig. 2B shows an IgG1-κ control microbubble (Ø = 3.3 μm) underneath the cell, with an internalized depth of −0.5 μm, and without any apparent alteration of the cell membrane (Supplementary Fig. 2B). Fig. 2C shows an $\alpha_v\beta_{3\text{-under}}$ microbubble (Ø = 5.0 μm) that is localized between the two cell membranes, with an internalized depth of 3.9 μm, and with a distinguishable green ring in the cell membrane around the microbubble (Supplementary Fig. 2C). In Fig. 2C(ii) and (iii) the apical cell membrane directly below the microbubble is poorly distinguishable because imaging is hampered by the gas core of the microbubble. Fig. 2D shows an $\alpha_v\beta_{3\text{-above}}$ microbubble (Ø = 3.9 μm) localized inside the cell, with an internalized depth of 3.1 μm, and with both a distinctive green ring and a dome in the cell membrane (Supplementary Fig. 2D). Fig. 2E shows a CD31$_{\text{under}}$ microbubble (Ø = 3.1 μm) underneath the cell, with an internalized depth of 0.8 μm, and with no distinguishably alteration of the cell membrane (Supplementary Fig. 2E). Finally, Fig. 2F shows a CD31$_{\text{above}}$ microbubble (Ø = 3.3 μm) above the cell, with an internalized depth of −0.1 μm, and with a distinguishably shadow on the cell membrane and CellMask Green dye-transfer around the microbubble shell (Supplementary Fig. 2F). In Fig. 2F(ii) and (iii) the cell membrane is again poorly distinguishable directly below the microbubble.

The $\alpha_v\beta_3$ microbubbles showed significantly ($p < 0.001$) more
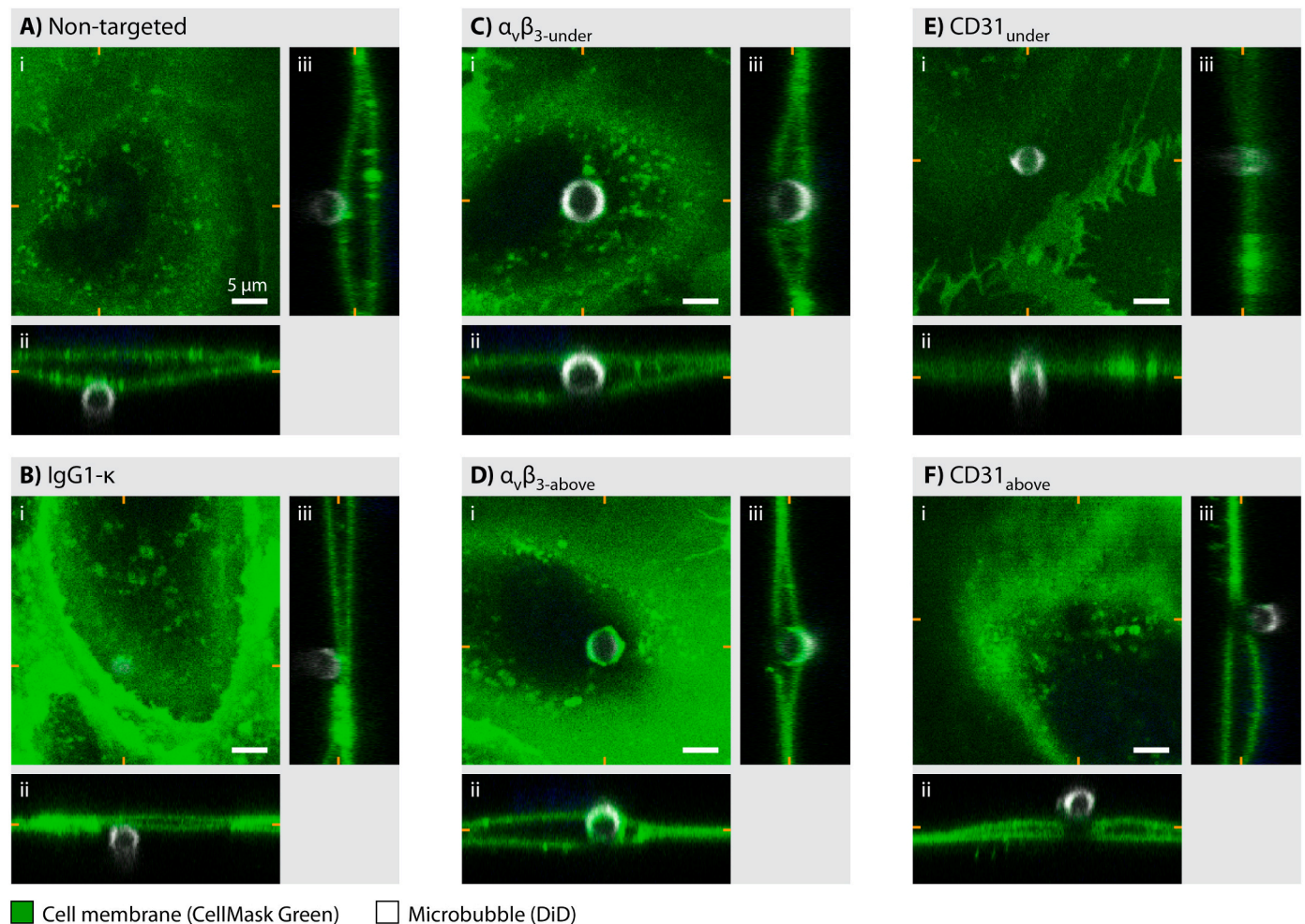

Fig. 2. Orthogonal views of typical examples of confocal microscopy z-stacks showing the 3D morphology of the endothelial cell membrane and microbubbles: A) non-targeted microbubble underneath the cell, B) IgG1-κ control microbubble underneath the cell, C) $\alpha_v\beta_{3\text{-under}}$ targeted microbubble underneath the cell, D) $\alpha_v\beta_{3\text{-above}}$ targeted microbubble above the cell, E) CD31$_{\text{under}}$ targeted microbubble underneath the cell, and F) CD31$_{\text{above}}$ microbubble above the cell. Side views have the objective imaging from (ii) above or (iii) the right. Orange markings indicate the cross-section of the orthogonal planes of the side views. See Supplementary Fig. 2 for only the CellMask Green channel of the same views. (For interpretation of the references to colour in this figure legend, the reader is referred to the web version of this article.)

internalization than any other type of microbubble, with a median (IQR between square brackets) internalized depth of 4.0 μm for $\alpha_v\beta_{3\text{-under}}$ and 3.0 μm for $\alpha_v\beta_{3\text{-above}}$ (Fig. 3A). The CD31$_{under}$ microbubbles, with an internalized depth of 0.9 μm, internalized significantly ($p < 0.001$) more than the CD31$_{above}$ microbubbles (-0.1 μm), non-targeted microbubbles (-0.1 μm), and IgG1-κ microbubbles (0.1 μm). The orientation of the microbubble with respect to the cell affected the internalized depth when comparing the same microbubble type. When the $\alpha_v\beta_3$ or CD31 microbubble was located underneath the cells the internalized depth

was significantly larger ($p < 0.001$) than when located above the cells.

In Fig. 3B the correlation between the internalized depth and cell thickness is shown for each microbubble type and set-up orientation. The internalized depth of $\alpha_v\beta_3$ microbubbles strongly correlated with the cell thickness [Fig. 3B(iii)], both for $\alpha_v\beta_{3\text{-under}}$ (Spearman's correlation coefficient $\rho = 0.89, p < 0.001$) and $\alpha_v\beta_{3\text{-above}}$ ($\rho = 0.69, p < 0.001$). This correlation appeared to weaken for the other microbubbles types with decreasing internalized depths, showing a moderate correlation for CD31$_{under}$ microbubbles ($\rho = 0.57, p < 0.001$) [Fig. 3B(iv)]. A weak
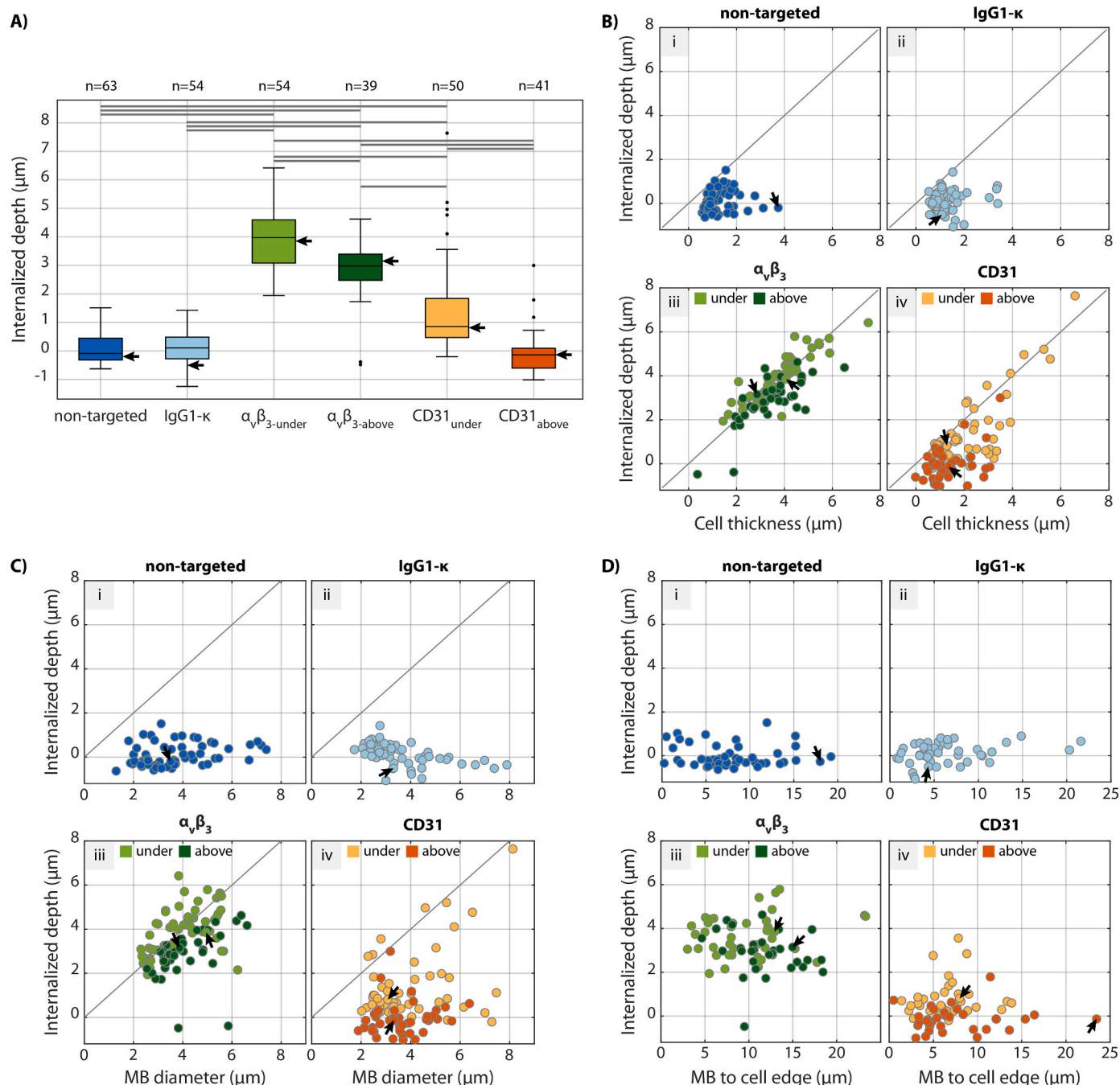
Fig. 3. Internalized depth of microbubbles into endothelial cells for non-targeted microbubbles (dark blue), IgG1-κ control microbubbles (light blue), $\alpha_v\beta_{3\text{-under}}$ targeted microbubbles (light green), $\alpha_v\beta_{3\text{-above}}$ targeted microbubbles (dark green), CD31$_{under}$ targeted microbubbles (yellow), CD31$_{above}$ targeted microbubbles (orange). A) Internalized depth for the distinct microbubble types and experimental set-up orientations; statistically significant differences indicated by horizontal lines (all at $p < 0.001$, i.e. $p < 6.67e\text{-}05$ after Bonferroni correction). B) Internalized depth as a function of cell thickness. C) Internalized depth as a function of microbubble (MB) diameter. D) Internalized depth as a function of the distance from the microbubble to the nearest cell edge. In all plots the arrows indicate the data points corresponding to the typical examples of Fig. 2. (For interpretation of the references to colour in this figure legend, the reader is referred to the web version of this article.)

correlation was found for the categories that had a median internalized depth ≤ 0.1 μm, which was significant for non-targeted microbubbles ($\rho = 0.26$, $p < 0.05$) and non-significant for CD31$_{above}$ ($\rho = 0.26$, $p = 0.1$) and IgG1-κ ($\rho = 0.11$, $p = 0.4$) microbubbles. An overview of all correlation coefficients between internalized depth and cell thickness is given in Supplementary Table 2.

To further investigate internalization, we can compare the scatter plots of $\alpha_v\beta_3$ microbubbles in Fig. 3B(iii) and of CD31 microbubbles in Fig. 3B(iv). It becomes apparent that there are more CD31 microbubbles with an internalized depth smaller than the cell thickness (on the right bottom half of the graph), than for $\alpha_v\beta_3$ microbubbles. This indicates that there are more CD31 than $\alpha_v\beta_3$ microbubbles that do not completely fill the cell. If we normalize the internalized depth to the cell thickness, to quantify how much of the cell is filled with the microbubble, this is only 28% for CD31 microbubbles and indeed significantly ($p < 0.001$) lower than the 101% for $\alpha_v\beta_3$ microbubbles.

The cell thickness (Supplementary Fig. 3) was also evaluated for cells without a microbubble in both set-up orientations, i.e. with the cells under ($n = 21$) or above ($n = 12$) the CLINIcell membrane. The median cell thickness was 2.3 μm and 2.2 μm, respectively. There was no significant difference in cell thickness between these two orientations when there was no microbubble on the cell. The cell thickness found for $\alpha_v\beta_3$ microbubbles was significantly ($p < 0.001$) larger than that of any other type of microbubble.

In Fig. 3C the internalized depth is shown as a function of the microbubble diameter. The internalized depth of $\alpha_v\beta_3$ microbubbles correlated with the microbubble diameter, both for $\alpha_v\beta_{3-under}$ (Spearman's correlation coefficient $\rho = 0.50$, $p < 0.001$) and $\alpha_v\beta_{3-above}$ ($\rho = 0.62$, $p < 0.001$). Despite that this correlation was not significant for CD31 microbubbles, Fig. 3C(iv) does show that the CD31$_{under}$ microbubbles that are most internalized correspond to those with the largest diameter. An overview of all correlation coefficients between the internalized depth and microbubble diameter is given in Supplementary Table 2.

Finally, Fig. 3D shows the relationship between internalized depth and the microbubble location on the cell, quantified as the distance between the microbubble and the nearest cell edge. There was no correlation between internalization and microbubble location for any of the microbubble types or set-up orientations, see detailed correlation coefficients in Supplementary Table 2.

The overall occurrence of the distinctive cell membrane morphological traits identified and described above (Fig. 2 and Supplementary Fig. 2), revealed that a shadow was found significantly ($p < 0.001$) more often for microbubbles above a cell ($\alpha_v\beta_{3-above}$ and CD31$_{above}$) and for $\alpha_v\beta_{3-under}$ than for the other microbubble types (CD31$_{under}$, non-targeted, IgG1-κ; Supplementary Fig. 4A(i)). In 24% of the CD31$_{under}$ microbubbles a shadow was identified, which corresponded to the most internalized microbubbles: the internalized depth of CD31$_{under}$ with a shadow was significantly ($p < 0.001$) larger than those not exhibiting a shadow, as shown in Supplementary Fig. 4A(ii). Green rings were found significantly ($p < 0.001$) more often for $\alpha_v\beta_3$ and CD31 microbubbles than for IgG1-κ or non-targeted microbubbles (Supplementary Fig. 4B). Domes were found for 33% of all $\alpha_v\beta_3$ and CD31 microbubbles, but significantly ($p < 0.001$) more often for the $\alpha_v\beta_{3-above}$ microbubbles (79%) than for any other type or orientation (Supplementary Fig. 4C). Finally, dye-transfer was found significantly ($p < 0.001$) more often for CD31$_{above}$ microbubbles than any other type and orientation (Supplementary Fig. 4D). When either a dome or dye-transfer was identified in the xz- or yz-plane, most often also a green ring was identified in the xy-plane (striped areas in Supplementary Fig. 4C and D).

3.2. Acoustic behavior

After 3D imaging of the initial microbubble-cell configuration, for 246 of these FOVs the microbubble's excursion upon ultrasound insonification was recorded using the Brandaris 128 ultra-high-speed

camera, with $n \geq 32$ per microbubble type. The sample size per microbubble type and set-up orientation can be found in Supplementary Table 1. The ultra-high-speed imaging revealed that microbubble excursion amplitude was smaller when microbubbles were internalized (Fig. 4). In Fig. 4A, the microbubble excursion amplitude (R_{max}-R_0) is shown as a function of initial microbubble radius (R_0), where the scatter markers are colour-coded ranging from not internalized in blue to highly internalized in yellow. This colour-coded representation reveals the blue scatter points at higher excursion amplitudes than those colored in green/yellow tones, hence showing how a larger internalized depth led to a lower excursion amplitude. This is confirmed by the average excursion of non-internalized microbubbles (internalized depth < 1 μm, blue line) being consistently higher than that of internalized microbubbles (internalized depth ≥ 1 μm, yellow line). For microbubbles with R_0 up to 3.2 μm, statistical testing confirmed that the excursion amplitude was significantly higher for non-internalized microbubbles (internalized depth < 1 μm), as represented in Fig. 4B. Additionally, in Fig. 4A, the characteristic resonance behavior of microbubbles can be recognized, showing a slightly larger resonance radius for non-internalized microbubbles (2.4 μm, blue line) than for internalized microbubbles (2.2 μm, yellow line).

3.3. Drug delivery by pores or tunnels

After ultra-high-speed imaging of the microbubble oscillation behavior, the cellular response upon microbubble oscillation was evaluated for a total of 230 FOVs using time-lapse confocal microscopy, with $n \geq 31$ per microbubble type and set-up orientation (detailed sample size per category in Supplementary Table 1). Typical examples of the cellular responses are presented in Fig. 5, showing selected frames of confocal microscopy time-lapse imaging, the microbubble excursion, and time profiles of the perforated area and PI and CellMask Green intensity. Before ultrasound, confocal microscopy showed a single microbubble in each field view and revealed that each cell was viable and had an intact cell membrane (absence of PI).

Fig. 5A shows a typical example of PI uptake and distinguishable membrane perforation. The corresponding confocal microscopy recording is shown in Video S1. After ultrasound, high PI uptake was observed starting at the microbubble location and gradually spreading into the cell over time. Additionally, membrane perforation was identified as an area with decreased CellMask Green intensity, localized next to the microbubble. This perforated area increased to about 30 μm^2 during the first ~30s and then the pore remained open throughout the rest of the recording (the slight variation in perforated area is caused by focus drift throughout time-lapse live cell imaging). The 3D confocal microscopy image after the time-lapse recording, confirmed that there was still CellMask Green signal in the perforated area (Supplementary Fig. 5A). This indicates that there was still cell membrane present there, suggesting that only the apical membrane was perforated and that the basal membrane was still intact. This type of perforation will from now on be described as the formation of a *pore*.

In Fig. 5B another typical example is shown of PI uptake and visibly distinguishable membrane perforation. The corresponding confocal microscopy recording is shown in Video S2. After ultrasound insonification, again high PI uptake was observed to gradually fill the cell over time and membrane perforation was identified. The perforated area quickly increased to about 50 μm^2 within the first ~20s and then stabilized. However, in this case the CellMask Green signal seemed to have completely disappeared in the perforated area. This suggests that both the apical and the basal membrane had been perforated. This resulted into a transcellular perforation, as confirmed by the final 3D confocal microscopy (Supplementary Fig. 5B). This type of perforation will from now on be described as formation of a *tunnel*.

In Fig. 5C another typical example is shown of PI uptake and tunnel formation. The corresponding confocal microscopy recording is shown in Video S3. After ultrasound insonification, PI uptake was observed
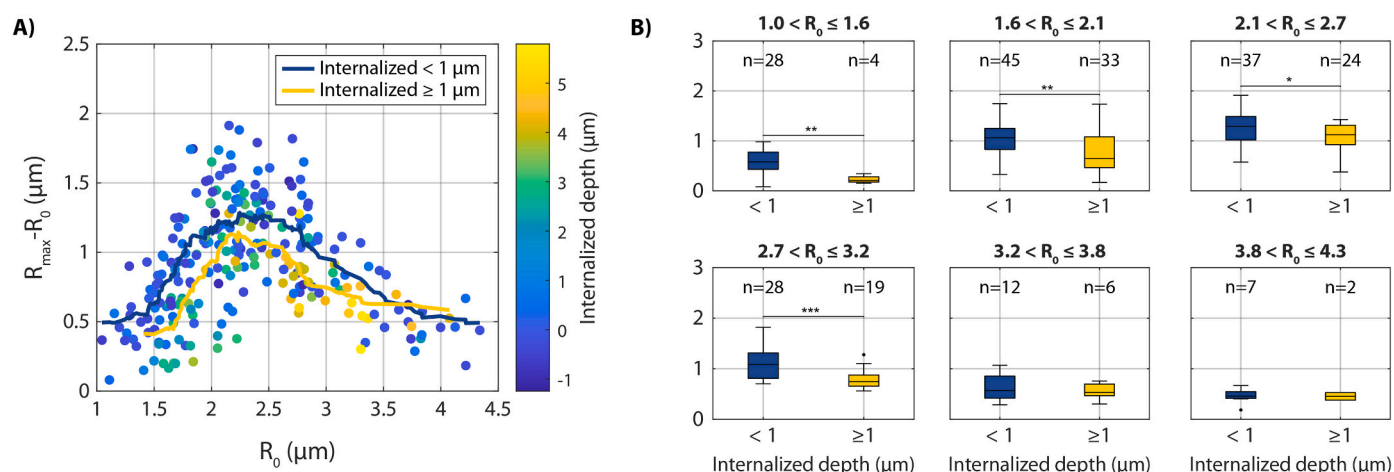
Fig. 4. Excursion amplitude and internalized depth. A) Microbubble excursion amplitude (R_{max}-R_0) as a function of initial microbubble radius (R_0) with scatter dots colour-coded corresponding to the internalized depth. The lines show the 20-point moving mean of the excursion amplitude for all microbubbles internalized <1 μm (blue) or ≥ 1 μm (yellow). B) Excursion amplitude of microbubbles internalized <1 μm (blue) or ≥ 1 μm (yellow) within ranges of similar microbubble size. (For interpretation of the references to colour in this figure legend, the reader is referred to the web version of this article.)
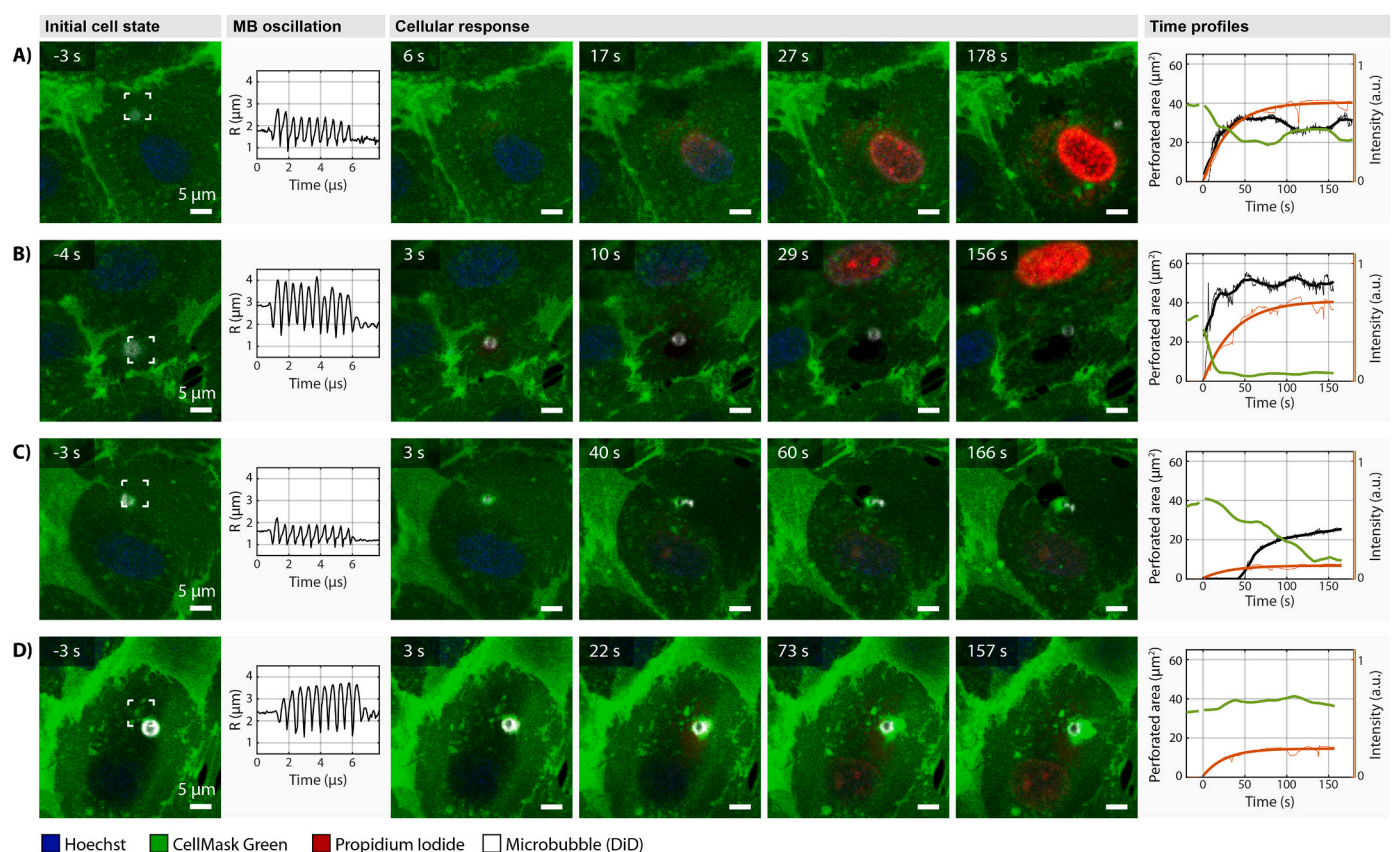
Fig. 5. Typical examples of microbubble-mediated drug delivery by pores and tunnels. A) High PI uptake and a distinguishable membrane perforation identified as a pore caused by an IgG1-κ microbubble (0.7 μm internalized depth). B) High PI uptake and distinguishable membrane perforation identified as a tunnel caused by a non-targeted microbubble (−0.1 μm internalized depth). C) Low PI uptake and distinguishable membrane perforation identified as a tunnel caused by a CD31$_{under}$ microbubble (1.0 μm internalized depth). D) Low PI uptake and no distinguishable membrane perforation caused by an $\alpha_v\beta_{3-\ under}$ microbubble (3.1 μm internalized depth). For every example the images from left to right show: one confocal microscopy frame showing the initial cell state before ultrasound; the microbubble (MB) radius as a function of time obtained from the Brandaris 128 ultra-high-speed imaging during ultrasound; four selected frames of confocal microscopy time-lapse imaging after ultrasound; and the time profiles () of the perforated area (black, thick line shows moving average), PI fluorescent intensity in the cell (red, thick line show fit to Eq. 1), and CellMask Green fluorescent intensity within the area indicated by the white corners in the initial cell state (green, thick line shows moving average). See Supplementary Fig. 5 for the 3D confocal microscopy imaging of these examples before and after time-lapse imaging. (For interpretation of the references to colour in this figure legend, the reader is referred to the web version of this article.)

immediately but in contrast to the previous examples, it stabilized at a low level. At 45 s after ultrasound, the perforated area became distinguishable in the confocal microscopy time-lapse image and gradually increased to about 25 μm^2, with no remaining CellMask Green signal in the perforated area, indicating the formation of a *tunnel*. This transcellular perforation was again confirmed by the final 3D confocal microscopy (Supplementary Fig. 5C). The confocal microscopy images and the time profile of the PI intensity in the cell (red curve) indicate noticeably lower PI uptake in Fig. 5C than that in Fig. 5A and B, despite that in all three cases the membrane perforation clearly remained at the end of time-lapse imaging and was of similar size (black curve). This suggests that in Fig. 5C the initial intracellular perforation allowing uptake of PI from the extracellular space into the cytoplasm resealed and only a transcellular perforation (i.e. *tunnel*) remained. The difference between the perforated areas classified as a *pore* or a *tunnel* is clearly confirmed by the time profile of the CellMask Green intensity: for a pore (Fig. 5A) the intensity decreased to 54% of the fluorescent intensity before ultrasound, while for the tunnel it decreased to only 13% (Fig. 5B) or 20% (Fig. 5C) of the initial fluorescent intensity.

Finally, in Fig. 5D a typical example is shown of PI uptake without distinguishable membrane perforation. The corresponding confocal microscopy recording is shown in Video S4. After ultrasound, PI uptake was observed to gradually fill the cell while stabilizing at a low level. However, in this case no area of decreased CellMask Green intensity could be identified that would indicate membrane perforation (Supplementary Fig. 5D). This indicates that a *pore* was formed by the oscillating microbubble, causing PI uptake, but that it resealed too quickly, was too small to be identified with the CellMask Green dye and current imaging resolution, or concealed by the internalized microbubble.

The uptake of PI and the perforation of the cellular membrane was monitored, revealing four distinct responses: 1) no PI uptake and no distinguishable membrane perforation, 2) PI uptake with a distinguishable membrane perforation identified as a pore (Fig. 5A), 3) PI uptake with a distinguishable membrane perforation identified as a tunnel (Fig. 5B and C), and 4) PI uptake without distinguishable membrane perforation (Fig. 5D).

The occurrence of tunnels upon sonoporation was lower for $\alpha_v\beta_3$ microbubbles (0% of sonoporated cells for $\alpha_v\beta_{3\text{-under}}$ and 11.5% for $\alpha_v\beta_{3\text{-above}}$) than for the other types of microbubbles (25.0% of sonoporated cells for non-targeted, 17.9% for IgG1-κ, 26.1% for CD31$_{under}$, and 34.8% for CD31$_{above}$) (Fig. 6, blue). Additionally, $\alpha_v\beta_3$ microbubbles

resulted in PI uptake with invisible pores upon sonoporation more often (93.3% of sonoporated cells for $\alpha_v\beta_{3\text{-under}}$ and 80.8% for $\alpha_v\beta_{3\text{-above}}$), than for any other type of microbubble (12.5% of sonoporated cells for non-targeted, 28.6% for IgG1-κ, 26.1% for CD31$_{under}$, and 56.5% for CD31$_{above}$) (Fig. 6, light red).

In Fig. 7A, the amount of PI uptake is shown as a function of the perforated area, evaluated 120 s after ultrasound insonification. This quantification reveals that for $\alpha_v\beta_3$-targeted microbubbles the perforated area upon PI uptake was small and often not distinguishable [Fig. 7A(iii)]. PI uptake took place; however, the membrane disruption could often not be identified (see typical example in Fig. 5D). For the other types of microbubbles, sonoporation with a large pore (red, perforated area > 20 μm^2) always resulted in high PI uptake [Fig. 7A (i), (ii), and (iv)]. On the other hand, sonoporation with a large tunnel (blue, perforated area > 20 μm^2) led to both high and low PI uptake (Fig. 7A). This indicates that upon tunnel formation PI uptake sometimes stabilized early on, suggesting resealing of the membrane, while the transcellular perforation (i.e. tunnel) remained open (Fig. 11B iii). Overall, Fig. 7B reveals that microbubbles internalized by at least 1 μm, created significantly ($p < 0.001$) smaller perforated areas upon sonoporation.
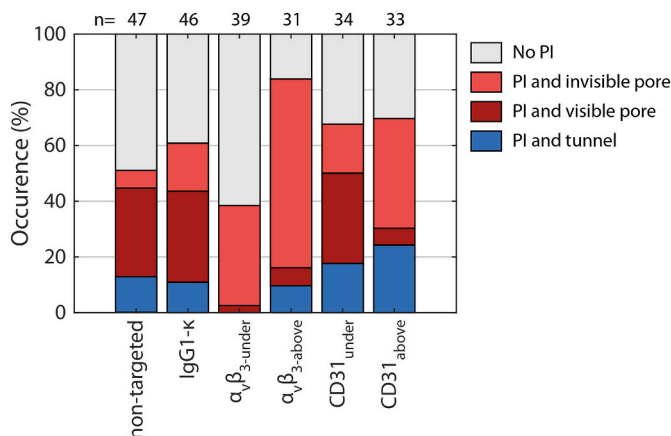
The median (IQR between square brackets) internalized depth of microbubbles that caused sonoporation with a tunnel was 0.0 [−0.3–0.6] μm and significantly ($p < 0.01$) smaller than that of microbubbles that caused sonoporation with a pore (0.6 [0.0–2.8] μm) (Fig. 7C). The thickness (1.1 [0.8–1.4] μm) of cells in which tunnels were caused was significantly ($p < 0.001$) smaller than that of cells with pores (1.7 [1.1–3.2] μm) or without sonoporation (1.7 [1.0–2.9] μm) (Fig. 7D). Additionally, tunnels were caused by microbubbles that were significantly closer to the cell edge than those that caused a pore or no sonoporation (Fig. 7E). Finally, there was no significant difference between the excursion amplitude of microbubbles that caused pores or tunnels (Supplementary Fig. 6A), but in both cases the excursion amplitude was significantly ($p < 0.001$) higher than the amplitude of the microbubbles that caused no sonoporation.

The threshold for sonoporation was lower for $\alpha_v\beta_3$ targeted microbubbles (R_{max}-R_0 = 0.7 μm) than for CD31, IgG1-κ, or non-targeted microbubbles (R_{max}-R_0 = 0.9 μm) (Fig. 8). The response appeared more predictable when the $\alpha_v\beta_3$ microbubble was above the cell, since 24 out of 24 microbubbles above the threshold caused sonoporation for $\alpha_v\beta_{3\text{-above}}$, but only 12 out of 20 microbubbles that oscillated above the threshold caused sonoporation for $\alpha_v\beta_{3\text{-under}}$.
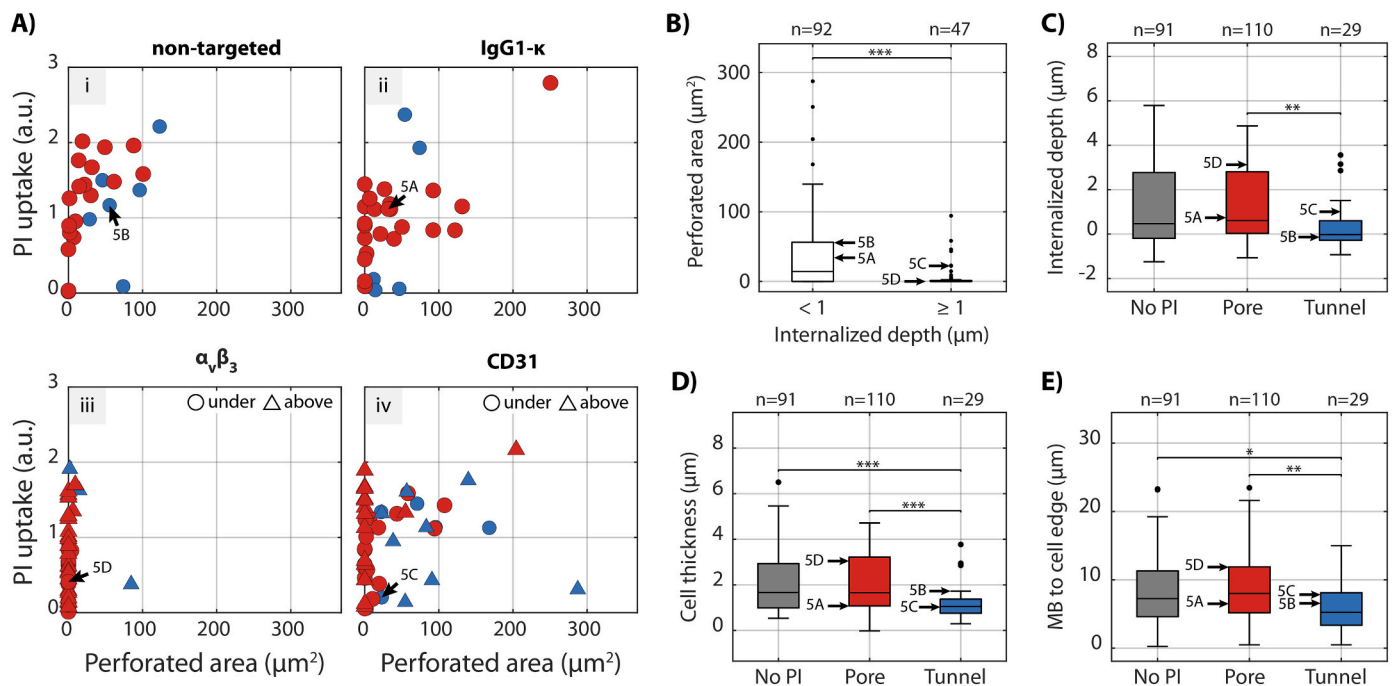
The size coefficients (α) and resealing coefficients (β) obtained from fitting the PI uptake profiles to Eq. (1) are shown for pores (Fig. 9A) and tunnels (Fig. 9B). *Non-resealing* intracellular perforations (Fig. 9, gray), indicating irreversible sonoporation, occurred notably more often for pores (64 out of 111 [58%]) than for tunnels (2 out of 28 [7%]). Additionally, two clear sub-categories were identified: *resealing* (Fig. 9, orange; 18 out of 111 pores [16%], 10 out of 28 tunnels [36%]) and *saturated* (Fig. 9, purple; 29 out of 111 pores [26%], 16 out of 28 tunnels [57%]). For both pores and tunnels the relative occurrence of these sub-categories was the same, since *saturated* perforations were found to occur 1.6× more often than *resealing* perforations. The low and stabilizing PI uptake curves of Fig. 5C and D correspond to *resealing* perforations, indicating reversible sonoporation, while the high and stabilizing PI uptake curves of Fig. 5A and B correspond to *saturated* perforations, suggesting severe cell damage upon sonoporation.

Fig. 6. Occurrence of drug delivery and cellular responses upon microbubble oscillation: no PI uptake (gray), PI uptake without distinguishable membrane perforation identified as invisible pore (light red), PI uptake with a distinguishable membrane perforation identified as visible pore (dark red), and PI uptake with a distinguishable membrane perforation identified as a tunnel (blue). (For interpretation of the references to colour in this figure legend, the reader is referred to the web version of this article.)

3.4. Principal component analysis

To explore the influence of the different parameters on microbubble internalization, drug delivery outcome and cellular response, a principal component analysis was performed of which the results are presented in Table 1 and Fig. 10. The first principal component (PC1) is dominated by the microbubble excursion amplitude, cell thickness, and internalized depth. The second principal component (PC2) is dominated by the microbubble excursion amplitude and distance from the microbubble to

Fig. 7. Cellular response upon microbubble oscillation either resulting in no propidium iodide (PI) uptake (gray, $n = 91$) or causing PI uptake with pores (red, $n = 111$) or tunnels (blue, $n = 28$). A) Amount of propidium iodide (PI) uptake upon sonoporation as a function of the perforated cell membrane area at 120 s after ultrasound for i) non-targeted microbubbles, ii) IgG1-targeted microbubbles, iii) $\alpha_v\beta_3$-targeted microbubbles, and iv) CD31-targeted microbubbles, with circles for MB on the bottom of the cell and triangle, above. B) Perforated area of sonoporated cells caused by microbubbles with an internalized depth < 1 or ≥ 1 μm. C) Internalized depth of microbubbles leading to the various cellular responses. D) Cell thickness at the microbubble location for each cellular response. E) Distance from the microbubble to the cell edge for each cellular response. The arrows indicate the data points corresponding to the typical examples of Fig. 5. In Supplementary Fig. 6 the data in C-E is presented per microbubble type. (For interpretation of the references to colour in this figure legend, the reader is referred to the web version of this article.)

the nearest cell edge. The loading plot in Fig. 10A visualizes these components.

In Fig. 10B, the PCA scoring and loading plot show the distribution of the different microbubble types and set-up orientations. The $\alpha_v\beta_3$ targeted microbubbles (light and dark green) are clearly shifted towards the right of the plot, towards the PC1 > 0. Based on the variable loading (Table 1), that means that $\alpha_v\beta_3$ microbubbles exhibit lower microbubble excursion amplitudes, higher internalized depths, larger distances from the cell edge, and higher cell thicknesses than any of the other microbubble types. In Fig. 10C, the PCA scoring is shown for the different drug delivery outcomes. The occurrence of sonoporation with distinguishable pores (red) is shifted towards both the top and left quadrants of the plot, corresponding to the higher excursion amplitudes. The occurrence of sonoporation with tunnels (blue) is shifted more towards the left (PC1 < 0), corresponding to lower internalized depths, smaller distance from the cell edge, and lower cell thickness.

4. Discussion

The 3D morphology of the endothelial cell membrane adjacent to microbubbles was evaluated for non-targeted, $\alpha_v\beta_3$-targeted, CD31-targeted, and IgG1-κ control microbubbles. The $\alpha_v\beta_3$ microbubbles were most internalized, with a median internalized depth of 3 μm when above and 4 μm when under the cell, while for CD31 microbubbles internalization was only significant when the microbubble was under the cell (0.9 μm). Since non-targeted and IgG1-κ control microbubbles showed negligible internalized depths (≤ 0.1 μm), internalization appeared to be a receptor-mediated mechanism. Furthermore, the influence of microbubble internalization on the drug delivery outcome and cellular response was investigated by recording the microbubble oscillation at ultra-high temporal resolution and subsequent model drug uptake and membrane perforation in 2D and 3D at high-spatial

resolution. Different cellular responses were observed with sonoporation occurring by formation of pores and tunnels. The sonoporation threshold was lower for $\alpha_v\beta_3$ microbubbles than for all other microbubble types, signifying that the 3D morphology of the endothelial cell membrane upon microbubble internalization and the resulting microbubble oscillation affected the drug delivery outcome.

4.1. Internalized targeted microbubbles

For a better understanding of microbubble internalization, the correlations between internalized depth and other parameters – cell thickness, microbubble size, and microbubble distance to cell edge – were explored in more detail (Fig. 3). While there was no clear correlation between the microbubble distance to cell edge and the internalized depth, the cell thickness and microbubble size both correlated with the internalized depth, especially for $\alpha_v\beta_3$ microbubbles. Cell thickness was larger when microbubbles were more internalized and when compared to the control cells without microbubbles. Moreover, the larger the microbubble, the higher the internalized depth. Hence, it appeared that $\alpha_v\beta_3$ microbubbles were fully internalized into the cell, with the cell membrane covering the internalized microbubbles entirely and resulting in thickening of the cells (Fig. 11A iii, iv). This can be observed in the typical examples shown in Fig. 2C and D (Supplementary Fig. 2C and D) and often resulted into dome formation (Fig. 2D) when the cell membrane covered a microbubble that was larger than the cell thickness (Fig. 11A iv).

The orientation of the set-up, being microbubble under the cell or microbubble above the cell, also affected the internalized depth. Both $\alpha_v\beta_3$ and CD31 microbubbles located above the cells were significantly less internalized than the same type of microbubble located underneath the cell. This can be explained by buoyancy, since despite the fact that the microbubble is internalized when it is located above the cells it tends
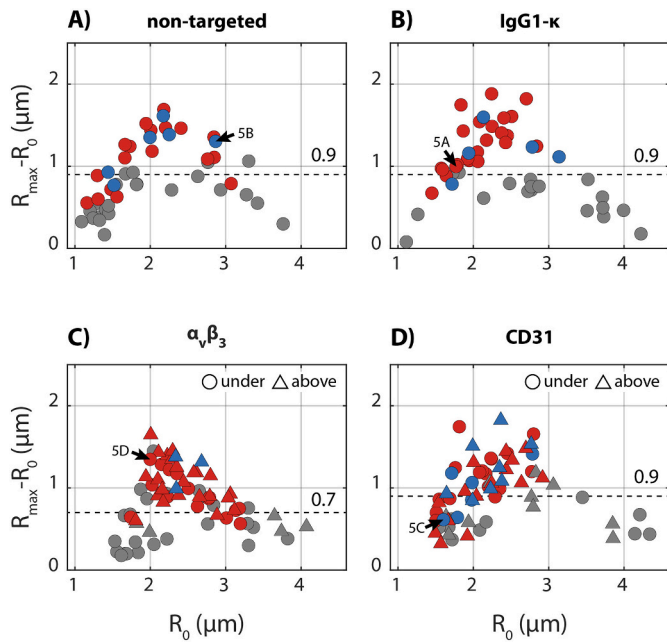
Fig. 8. Microbubble excursion and drug delivery outcome resulting in no PI uptake (gray), sonoporation with pores (red), or sonoporation with tunnels (blue) for all microbubble types: A) non-targeted, B) IgG1-κ, C) $\alpha_v\beta_3$-under (circles) and $\alpha_v\beta_3$-above (triangles), D) CD31-under (circles) and CD31-above (triangles). All plots show microbubble excursion amplitude ($R_{max}-R_0$) as a function of microbubble resting radius (R_0). Sonoporation threshold indicated by the dotted line and the number. The arrows indicate the data points corresponding to the typical examples of Fig. 5. See Supplementary Fig. 6A for statistical comparison between drug delivery outcome categories. (For interpretation of the references to colour in this figure legend, the reader is referred to the web version of this article.)
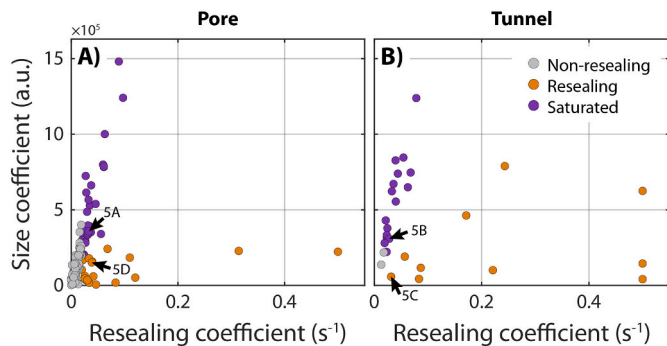
Fig. 9. Perforation size and resealing coefficients for A) pores and B) tunnels and the resulting classification as non-resealing (gray), resealing (orange), and saturated (purple). The arrows indicate the data points corresponding to the typical examples of Fig. 5. (For interpretation of the references to colour in this figure legend, the reader is referred to the web version of this article.)

Table 1

Scores of principal component analysis of microbubble excursion amplitude ($R_{max}-R_0$), internalized depth, distance between microbubble and nearest cell edge, and cell thickness. The scores indicate the weight of each variable in the PCA component.

	PC1	PC2
Microbubble excursion	−0.4239	2.2570
Internalized depth	0.3850	−0.0364
Distance to cell edge (MB-cell)	0.0829	0.1005
Cell thickness	0.5119	−0.0062

to float upwards, thereby slightly 'pulling' itself out of the cells causing lower internalized depths (Fig. 11A iv). In this orientation the formation of domes upon internalization ($\alpha_v\beta_3$-above) was observed more often, confirming that the cell membrane lined the internalized microbubble. Vice versa, when the microbubble was underneath the cell, it would float upwards 'pushing into' the cell, hence favoring a greater internalized depth. By studying microbubbles internalization in two orientations, we were able to properly visualize the basal cellular membrane when the microbubble was located under the cell or properly visualize the apical cellular membrane when the microbubble was above the cell, thereby still providing us with a complete picture of the internalization morphology.

No difference was found between internalized depth measured after about 10 min, i.e. the first microscopy imaging time point, compared to after 2 h after adding the microbubbles to the cells. This indicates that internalization of microbubbles by endothelial cells occurred within 10 min upon targeted microbubbles coming into contact with the cellular receptors, instead of progressing over a longer time window. This is in agreement with the previously found timescales of internalization (5–15 min) of similarly-sized particles by HUVEC and of microbubbles by leukocytes [41,42].

Distinct morphological traits in the cell membrane were monitored, being the occurrence of a shadow or green ring at the microbubble location, and dome formation or dye-transfer from the cell membrane to the microbubble coating. When the microbubble was under the cell, observation of a shadow indicated microbubble internalization ($\alpha_v\beta_3$-under and CD31-under, Supplementary Fig. 4). The appearance of a shadow in the endothelial cell membrane was related to the internalized depth of the microbubble. When the microbubble was above the cell ($\alpha_v\beta_3$-above and CD31-above), a shadow was found irrespective of internalization, explained by the microbubble's gas core having a different breaking index than the surrounding medium, resulting in a decreased fluorescent signal. In the case of dome formation, it appeared as if the cell membrane fully covered the microbubble, which was noticeably different from the occurrence of dye-transfer, where only some spots of cell membrane dye were visible on the microbubble shell. Based on our results it is not possible to distinguish between the transfer of dye only, or the transfer of membrane lipids into the microbubble coating bringing the fluorescent dye molecules along. Dye transfer was observed for IgG1-κ control, non-targeted, and CD31 microbubbles, but not for $\alpha_v\beta_3$ microbubbles. This suggests that the process of dye or lipid transfer was not solely receptor-mediated. Since dome formation was often observed for $\alpha_v\beta_3$ microbubbles, perhaps dye transfer was inhibited or obscured by complete internalization of the microbubble by the endothelial cell. Finally, green rings were observed for the majority of $\alpha_v\beta_3$ and CD31 microbubbles, but notably less observed for the non-targeted and IgG1-κ control microbubbles. The occurrence of this highly fluorescent ring might be due to the rearrangement of membrane lipids, which could become more tightly packed around the microbubble location resulting in an increased concentration of dye.

Previous work that focused on internalization of microbubbles by macrophages and endothelial cells showed that while macrophages efficiently internalized polyvinyl-alcohol-coated microbubbles, endothelial cells did not [43]. This is in agreement with the non-targeted and IgG1-κ control groups, which were not internalized in our study. To the best of our knowledge, internalization by endothelial cells of microbubbles targeted to specific receptors has not been investigated before; although the endothelial cell receptors $\alpha_v\beta_3$-integrin and CD31 have been investigated extensively. HUVECs cultured under flow are able to internalize submicron-sized membrane vesicles with a mechanism involving $\alpha_v\beta_3$-integrin [44], which is in line with our observations of $\alpha_v\beta_3$-targeted microbubbles being internalized.

The CD31-targeted microbubbles adhered to the endothelial cells by binding to CD31, also known as PECAM-1. Similar sized particles, such as *Plasmodium falciparum*-infected erythrocytes, also adhere to PECAM-1, but were suggested to be too large for internalization [45]. Different
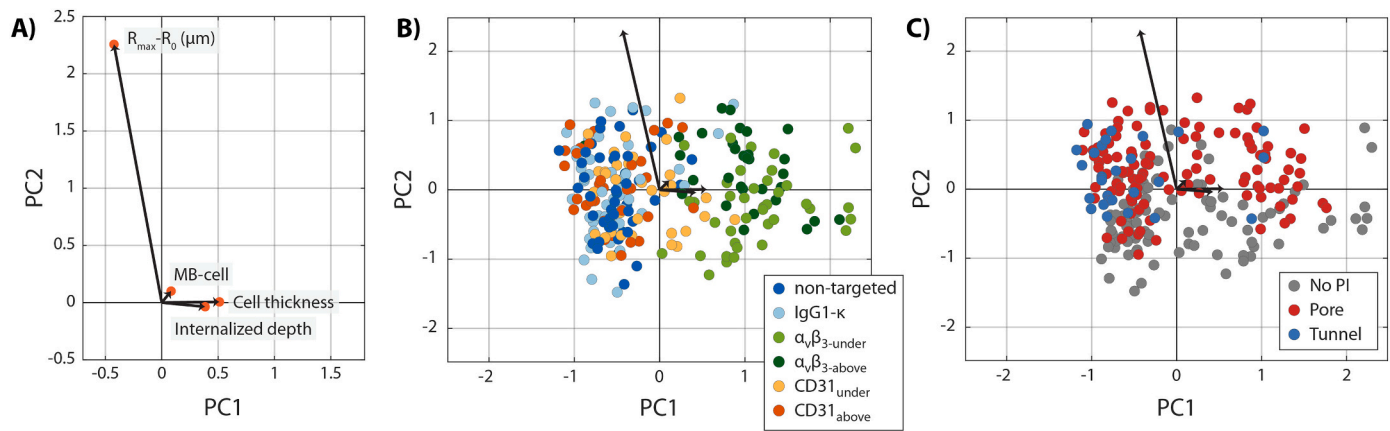
Fig. 10. Principal component analysis (PCA) of the microbubble excursion amplitude (R_{max}-R_0), internalized depth, cell thickness at the microbubble location, and distance from the microbubble to the cell edge (MB-cell). A) PCA loading plot, with the first principal component (PC1) explaining 51.4% of the variance and the second principal component (PC2) explaining 25.7% of the variance. B) PCA loading plot and scores colour-based on the microbubble type and orientation. C) PCA loading and scores colour-based on the drug delivery outcome: no PI uptake (gray), sonoporation with a pore (red), and sonoporation with a tunnel (blue). (For interpretation of the references to colour in this figure legend, the reader is referred to the web version of this article.)
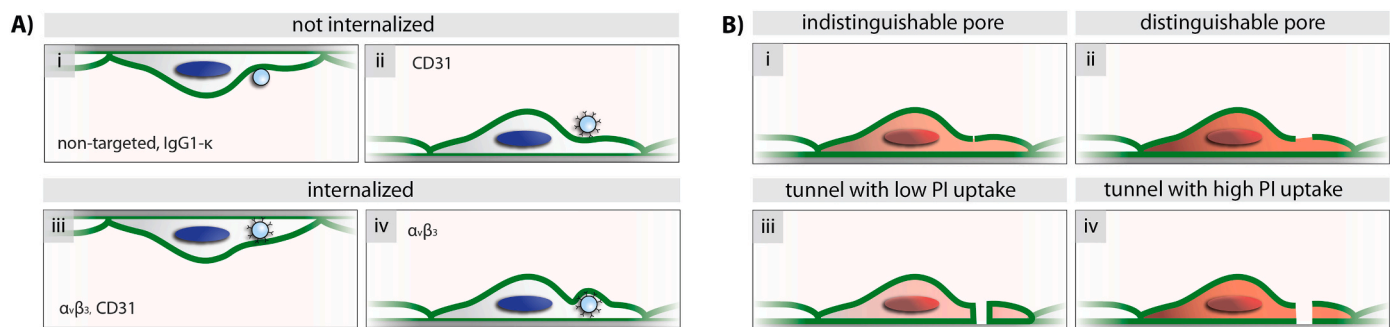
Fig. 11. Schematic representation of the observed 3D microbubble-endothelial cell dynamics. A) Microbubble-cell morphology showing the microbubble (i) under or (ii) above the cell and a targeted microbubble internalized (iii) under or (iv) above the cell. B) Cellular response and drug delivery outcome resulting in PI uptake by (i) an indistinguishable perforation, (ii) a distinguishable perforation, (iii) a tunnel with low PI uptake due to resealing of the membrane while the tunnel remains open and (iv) a tunnel with simultaneous membrane perforation leading to high PI uptake.

ligand-dependent pathways have been shown to facilitate internalization of smaller particles (100–300 nm in diameter) by HUVECs through PECAM-1 binding [46]. Since for CD31 microbubbles internalization was only significant when the microbubble was located under the cell and to a lesser extent than for $\alpha_v\beta_3$ microbubbles, it is possible that internalization for CD31 was partly driven by the buoyancy of the microbubble. Although non-targeted and IgG1-κ microbubbles were studied under this same orientation, internalization was not observed. Hence, internalization of $\alpha_v\beta_3$ and CD31 microbubbles appeared to be a combined result of an orientation- and ligand-driven process.

Previous work on the phagocytosis of microbubbles found that non-targeted phospholipid-coated microbubbles were phagocytosed by leukocytes through opsonization of the complement component C3/C3b [42]. However, in the current study non-targeted microbubbles were not internalized by HUVECs, hence it is unlikely that complement factors binding to the microbubble surface or ligand play a role in the internalization of targeted microbubbles by HUVECs.

4.2. Drug delivery outcome by pores and tunnels

The acoustic response of individual microbubbles was recorded with ultra-high-speed imaging to determine the acoustic behavior and its effect on the drug delivery outcome. The excursion amplitude and resonance size were lower for internalized microbubbles. This suggests an increase in viscous damping, which is in agreement with the decreased oscillation observed by high-speed streak imaging of

phagocytosed MP1950 microbubbles in neutrophils [47].

After microbubble oscillation, sonoporation identified by PI uptake and a frequently coinciding distinguishable cell membrane perforation were observed (Fig. 5). In the distinguishable perforated areas, the level of fluorescence signal in the CellMask Green channel was either half of the pre-insonification level or approaching zero. Since the distance between the apical and basal membrane is very small for endothelial cells, signal from both membranes could be detected with the limited axial-resolution of the current 2D imaging set-up. Therefore, a partial decrease of CellMask Green signal indicated that only one of the membranes was perforated. This interpretation of the 2D images was confirmed by the 3D imaging performed at the end, as shown in Supplementary Fig. 5. Hence, in 2D confocal microscopy time-lapse imaging, a distinction could be made between *pore* formation, where only the apical cell membrane was perforated, and *tunnel* formation, where both the apical and basal cell membranes were perforated. These different cellular effects can lead to either intracellular delivery with or without a distinguishable pore (Fig. 11B i, ii), transcellular delivery through a tunnel with limited intracellular delivery (Fig. 11B iii), or both intracellular and transcellular delivery occurring simultaneously (Fig. 11B iv). The occurrence of tunnels or pores was affected by different factors such as the orientation, internalized depth, cell thickness, microbubble distance to the cell edge, and the excursion amplitude (Fig. 7 and Fig. 8). Tunnels occurred more often when the microbubble was closer to the cell edge (Fig. 7). This could just be a mechanical effect because the cell is thinner there, as confirmed by tunnels occurring more often at thinner

cell locations (Fig. 7). However, it could also be enhanced by a biological mechanism, e.g., neutrophils are known to migrate towards the cell edge for extravasation [48,49].

The reversibility of sonoporation was assessed based on the PI uptake curves. Intracellular perforations not resealing within 120 s (i.e. *non-resealing*) are known to correlate with loss of cell viability [40]. Additionally, intracellular perforations classified as *saturated* are indicative of severe cell damage and suggestive of cell death [9,12]. Hence, if we consider both *non-resealing* and *saturated* perforations to cause cell death, cells remained viable less often upon pore formation (16%) than upon tunnel formation (36%). However, this only evaluates cell viability based on the resealing of the intracellular perforation and does not take into account the effect of a remaining transcellular perforation. Helfield et al. [10] showed resealing of a tunnel to occur on timescales up to 15 min after ultrasound, suggesting that in the current study resealing of a transcellular perforation might have been missed due to the limited timescale (up to 2.5 min). Additionally, recovery after enhancement of vascular permeability (i.e. transcellular perforation) has been shown to occur within 24 h in the blood-brain-barrier [50]. Hence, although a resealing intracellular perforation is at least required for cell viability, more long-term cellular mechanisms seem to play a role in recovery after tunnel formation. Therefore, cell faith after a transcellular perforation remains to be further investigated.

Tunnels upon microbubble oscillation, also known as transcellular or transendothelial perforations or holes, have been previously identified in HUVECs upon insonification of non-targeted DSPC-based microbubbles [10]. This is in agreement with the tunnel formation by non-targeted microbubbles we observed in the current study. Additionally, we found tunnel formation by targeted microbubbles. The range of perforated areas of tunnels found in the current study (2–287 μm^2, at 200 kPa PNP) was comparable to those found previously (39–683 μm^2, at 100–800 kPa PNP) [10]. However, we additionally observed intracellular uptake via pores (perforations of only the apical membrane) or indistinguishable perforations, suggesting that there are multiple potential drug delivery pathways as opposed to only tunnel formation. The difference in cellular responses observed may be caused by the cell culture chamber: for the present study the acoustically compatible CLINIcell [32] with 50 μm thick membranes was used in contrast to the glass-bottom dishes used in the previous study [10]. This highlights the importance of the *in vitro* model, in this case the surface on which endothelial cells are cultured, and how a model more analogous to the *in vivo* situation may lead to more translatable results.

When a CD31-targeted microbubble was located above the cell, the higher occurrence of sonoporation with an indistinguishable perforation may partly be explained by the microbubble orientation, since the gas core of a microbubble above the cell membrane could obscure pore formation. However, for other microbubble types the observed perforated areas were often much larger than the microbubble size, their imaging would therefore not have been fully hampered by the microbubble. Hence, it is more likely that the microbubble orientation influenced the microbubble-cell interaction resulting in smaller perforated areas upon sonoporation. The occurrence of transcellular perforations was the lowest for $\alpha_v\beta_3$-targeted microbubbles, both when under or above the cell. Additionally, the perforated area was smallest, and often even indistinguishable, for internalized microbubbles. This indicates that the microbubble-cell morphology prior to microbubble oscillation, including the internalized depth and dome formation, had a major effect on the cellular response. When pooling all types of microbubbles and orientations together, there was a significant difference in internalized depth, cell thickness, and microbubble location on the cell between pore and tunnel formation. The microbubble excursion amplitude was not significantly different between pore and tunnel outcomes, indicating that while a certain oscillation threshold must be reached to induce PI uptake, causing either pores or tunnels was not oscillation-driven within the studied range of excursion amplitudes. As the $\alpha_v\beta_3$-targeted microbubbles were the most internalized, the excursion amplitudes were

lower than for the other groups. However, the threshold for sonoporation was also lower for $\alpha_v\beta_3$-targeted microbubbles than for any other microbubble type, with a value of 0.7 μm in agreement with previous studies [9,12]. Hence, the different microbubble-cell interaction caused by internalized microbubbles increased the susceptibility to sonoporation.

A principal component analysis was performed to bring all different parameters influencing the drug delivery outcome and cellular response together. Microbubble excursion was an important determinant, which was negatively correlated to the internalized depth and cell thickness. Together with the rest of the data analysis, this again indicates that while the microbubble excursion is indeed an important factor in sonoporation, the drug outcome is also determined by the microbubble-cell interaction, including internalized depth, cell thickness, and the microbubble location on the cell. For less internalized microbubbles located closer to the cell edge tunnel formation, and thus transcellular delivery, is more likely to occur. However, the complex interaction between all different parameters ultimately determines which cellular response occurs.

4.3. Limitations and future perspectives

All experiments performed for this study were done *in vitro*, raising the question how the results translate to the *in vivo* situation. Human endothelial cells are a valid model to study vascular drug delivery, in the current study, however, cells were cultured in static conditions instead of under flow. This may influence the cellular responses and drug delivery outcome, as previous studies indicated that the susceptibility to sonoporation was significantly lower for HUVECs cultured under flow than for HUVECs cultured statically, while using the same ultrasound settings [51]. In practice, this difference in sonoporation threshold can be easily circumvented by increasing the acoustic pressure when translating to *in vitro* experiments under flow or an *in vivo* situation. Additionally, the different mechanical properties of the underlying cell substrate found *in vivo* may affect the microbubble's acoustic response [52–54]. Another consequence of the *in vitro* experimental method is the absence of immune cells, making it impossible to study the role of the immune response in the internalization of targeted microbubbles. Furthermore, if reducing internalization would be desired, that may be achieved by introducing a longer PEG tail to the microbubble formulation to reduce the immune recognition by creating a buried-ligand architecture, as previously described [22].

In the current study, drug delivery was monitored by uptake of PI, an established marker for sonoporation [13,31,39,55–57], because PI is only able to enter a viable cell after the membrane has been compromised and subsequently becomes fluorescent [58]. However, alternatives such as fluorescent dextrans or spheres may be more suitable as a model drug when interested in evaluating drug delivery of molecules of other sizes [59] than 1.23 by 0.92 nm for PI [60]. Additionally, PI is toxic in the long term once inside the cell [61]. Therefore, in the current study design it was not feasible to perform a post-treatment cell viability assay.

The microbubble targeting strategy used here may not be suitable for *in vivo* applications, as the streptavidin protein can induce an unwanted immune response [62,63]. However, several studies are ongoing to develop clinically translatable targeting strategies for microbubbles targeted to $\alpha_v\beta_3$ integrin [64–66]. The use of $\alpha_v\beta_3$-targeted microbubbles has been proposed for ultrasound molecular imaging of angiogenesis [67,68], however, up to now no studies have investigated the cellular response upon binding of $\alpha_v\beta_3$-microbubbles. Since our results indicate that endothelial cells are able to internalize $\alpha_v\beta_3$-targeted microbubbles *in vitro* under static conditions, it should be further investigated if this also occurs *in vivo*, and if so if this leads to endothelial cell activation and subsequent platelet adhesion as reported for HUVECs cultured under flow after internalization of submicron-sized membrane vesicles [44].

The results presented here reveal that the microbubble-cell

interaction stretches beyond a simple ligand-receptor binding, with the internalization of microbubbles playing a substantial role in the acoustic response and drug delivery outcome. We found significant differences in the internalization of microbubbles depending on the ligand, when comparing $\alpha_v\beta_3$ versus CD31-targeted microbubbles. This implicates the importance of investigating internalization by other ligands in the future, before choosing which ligand must be used for the desired outcome, such that the targeted microbubble formulation can be tailored to specific applications. For ultrasound molecular imaging lower oscillation amplitudes of internalized microbubbles may be undesirable, while for drug delivery applications the internalization of microbubbles might be favorable.

5. Conclusions

Investigating the 3D morphology of the endothelial cell membrane and adjacent microbubble revealed that microbubbles were internalized into the cell when targeted to $\alpha_v\beta_3$, irrespective of the initial microbubble-cell positioning, and when targeted to CD31 if the microbubble was initially positioned under the cell. Hence, microbubble internalization was found to be a receptor-mediated and buoyancy-enhanced cellular mechanism and correlated with cell thickness and microbubble size. Although internalized microbubbles exhibited lower excursion amplitudes upon insonification, the oscillation threshold for sonoporation was also lower than for non-internalized microbubbles, thus making cells with internalized microbubbles more susceptible to sonoporation. Evaluating the morphology of membrane perforation revealed that microbubble oscillation either caused a pore, when only the apical cell membrane was perforated resulting in intracellular drug delivery, or a tunnel, when both the apical and basal cell membrane were perforated resulting in intracellular drug delivery and a transcellular perforation. Internalized microbubbles caused less transcellular perforations and led to the smallest, or even indistinguishable, perforated areas. These novel insights demonstrate the influence of the microbubble internalization on the drug delivery outcome and thereby aid the development of the optimal therapeutic microbubble.

CRediT authorship contribution statement

Inés Beekers: Conceptualization, Methodology, Investigation, Formal analysis, Writing – original draft, Writing – review & editing. **Simone A.G. Langeveld:** Conceptualization, Writing – original draft, Writing – review & editing. **Bram Meijlink:** Investigation, Writing – review & editing. **Antonius F.W. van der Steen:** Supervision. **Nico de Jong:** Supervision, Writing – review & editing. **Martin D. Verweij:** Supervision, Writing – review & editing. **Klazina Kooiman:** Supervision, Conceptualization, Funding acquisition, Writing – review & editing.

Declaration of Competing Interest

The authors declare no conflict of interest.

Acknowledgments

Appendix A. Supplementary data

Supplementary data to this article can be found online at https://doi.org/10.1016/j.jconrel.2022.05.008.

References

[1] K. Kooiman, S. Roovers, S.A.G. Langeveld, R.T. Kleven, H. Dewitte, M.A. O'Reilly, J.-M. Escoffre, A. Bouakaz, M.D. Verweij, K. Hynynen, I. Lentacker, E. Stride, C. K. Holland, Ultrasound-responsive cavitation nuclei for therapy and drug delivery, Ultrasound Med. Biol. 46 (2020) 1296–1325, https://doi.org/10.1016/j.ultrasmedbio.2020.01.002.

[2] W.K. Chong, V. Papadopoulou, P.A. Dayton, Imaging with ultrasound contrast agents: current status and future, Abdom. Radiol. (New York). 43 (2018) 762–772, https://doi.org/10.1007/s00261-018-1516-1.

[3] K. Kooiman, H.J. Vos, M. Versluis, N. de Jong, Acoustic behavior of microbubbles and implications for drug delivery, Adv. Drug Deliv. Rev. 72 (2014) 28–48, https://doi.org/10.1016/j.addr.2014.03.003.

[4] I. Lentacker, I. De Cock, R. Deckers, S.C. De Smedt, C.T.W. Moonen, Understanding ultrasound induced sonoporation: definitions and underlying mechanisms, Adv. Drug Deliv. Rev. 72 (2014) 49–64, https://doi.org/10.1016/j.addr.2013.11.008.

[5] S. Roovers, T. Segers, G. Lajoinie, J. Deprez, M. Versluis, S.C. De Smedt, I. Lentacker, The role of ultrasound-driven microbubble dynamics in drug delivery: from microbubble fundamentals to clinical translation, Langmuir. 35 (2019) 10173–10191, https://doi.org/10.1021/acs.langmuir.8b03779.

[6] P. Qin, T. Han, A.C.H. Yu, L. Xu, Mechanistic understanding the bioeffects of ultrasound-driven microbubbles to enhance macromolecule delivery, J. Control. Release 272 (2018) 169–181, https://doi.org/10.1016/j.jconrel.2018.01.001.

[7] B. Helfield, A review of phospholipid encapsulated ultrasound contrast agent microbubble physics, Ultrasound Med. Biol. 45 (2019) 282–300, https://doi.org/10.1016/j.ultrasmedbio.2018.09.020.

[8] X. Duan, Q. Zhou, J.M.F. Wan, A.C.H. Yu, Sonoporation generates downstream cellular impact after membrane resealing, Sci. Rep. 11 (2021) 5161, https://doi.org/10.1038/s41598-021-84341-3.

[9] I. Beekers, F. Mastik, R. Beurskens, P.Y. Tang, M. Vegter, A.F.W. van der Steen, N. de Jong, M.D. Verweij, K. Kooiman, High-resolution imaging of intracellular calcium fluctuations caused by oscillating microbubbles, Ultrasound Med. Biol. 46 (2020) 2017–2029, https://doi.org/10.1016/j.ultrasmedbio.2020.03.029.

[10] B. Helfield, X. Chen, S.C. Watkins, F.S. Villanueva, Transendothelial perforations and the sphere of influence of single-site Sonoporation, Ultrasound Med. Biol. 46 (2020) 1686–1697, https://doi.org/10.1016/j.ultrasmedbio.2020.02.017.

[11] X. Chen, R.S. Leow, Y. Hu, J.M.F. Wan, A.C.H. Yu, Single-site sonoporation disrupts actin cytoskeleton organization, J. R. Soc. Interface 11 (2014) 20140071, https://doi.org/10.1098/rsif.2014.0071.

[12] I. Beekers, M. Vegter, K.R. Lattwein, F. Mastik, R. Beurskens, A.F.W. van der Steen, N. de Jong, M.D. Verweij, K. Kooiman, Opening of endothelial cell–cell contacts due to sonoporation, J. Control. Release 322 (2020) 426–438, https://doi.org/10.1016/j.jconrel.2020.03.038.

[13] B.L. Helfield, X. Chen, S.C. Watkins, F.S. Villanueva, Biophysical insight into mechanisms of sonoporation, Proc. Natl. Acad. Sci. 113 (2016) 9983–9988, https://doi.org/10.1073/pnas.1606915113.

[14] F. Forsberg, B.B. Goldberg, J.-B. Liu, D.A. Merton, N.M. Rawool, W.T. Shi, Tissue-specific US contrast agent for evaluation of hepatic and splenic parenchyma, Radiology. 210 (1999) 125–132, https://doi.org/10.1148/radiology.210.1.r99ja11125.

[15] P. Hauff, T. Fritzsch, M. Reinhardt, W. Weitschies, F. Lüders, V. Uhlendorf, D. Heldmann, Delineation of experimental liver tumors in rabbits by a new ultrasound contrast agent and stimulated acoustic emission, Investig. Radiol. (1997), https://doi.org/10.1097/00004424-199702000-00004.

[16] M.J. Blomley, T. Albrecht, D.O. Cosgrove, R.J. Eckersley, J. Butler-Barnes, V. Jayaram, N. Patel, R.A. Heckemann, A. Bauer, R. Schlief, Stimulated acoustic emission to image a late liver and spleen-specific phase of Levovist® in normal volunteers and patients with and without liver disease, Ultrasound Med. Biol. 25 (1999) 1341–1352, https://doi.org/10.1016/S0301-5629(99)00081-2.

[17] E. Quaia, M.J.K. Blomley, S. Patel, C.J. Harvey, A. Padhani, P. Price, D. O. Cosgrove, Initial observations on the effect of irradiation on the liver-specific uptake of Levovist, Eur. J. Radiol. 41 (2002) 192–199, https://doi.org/10.1016/S0720-048X(01)00458-2.

[18] K. Yanagisawa, F. Moriyasu, T. Miyahara, M. Yuki, H. Iijima, Phagocytosis of ultrasound contrast agent microbubbles by Kupffer cells, Ultrasound Med. Biol. 33 (2007) 318–325, https://doi.org/10.1016/j.ultrasmedbio.2006.08.008.

[19] M. Schneider, A. Broillet, P. Bussat, N. Giessinger, J. Puginier, R. Ventrone, F. Yan, Gray-scale liver enhancement in VX2 tumor-bearing rabbits using BR14, a new Ultrasonographic contrast agent, Investig. Radiol. 32 (1997) 410–417, https://doi.org/10.1097/00004424-199707000-00007.

[20] K.V. Ramnarine, K. Kyriakopoulou, P. Gordon, N.W. McDicken, C.S. McArdle, E. Leen, Improved characterisation of focal liver tumours: dynamic power Doppler imaging using NC100100 echo-enhancer, Eur. J. Ultrasound. 11 (2000) 95–104, https://doi.org/10.1016/S0929-8266(00)00074-4.

[21] A.K.P. Lim, N. Patel, R.J. Eckersley, S.D. Taylor-Robinson, D.O. Cosgrove, M.J. K. Blomley, Evidence for spleen-specific uptake of a microbubble contrast agent: a

quantitative study in healthy volunteers, Radiology. 231 (2004) 785–788, https://doi.org/10.1148/radiol.2313030544.

[22] C.C. Chen, M.A. Borden, The role of poly(ethylene glycol) brush architecture in complement activation on targeted microbubble surfaces, Biomaterials. 32 (2011) 6579–6587, https://doi.org/10.1016/j.biomaterials.2011.05.027.

[23] N.G. Fisher, J.P. Christiansen, A. Klibanov, R.P. Taylor, S. Kaul, J.R. Lindner, Influence of microbubble surface charge on capillary transit and myocardial contrast enhancement, J. Am. Coll. Cardiol. 40 (2002) 811–819, https://doi.org/10.1016/S0735-1097(02)02038-7.

[24] J. Aksnes, T.J. Eide, K. Nordstrand, Lipid entrapment and cellular changes in the rat myocard, lung and liver after long-term parenteral nutrition with lipid emulsion, APMIS. 104 (1996) 515–522, https://doi.org/10.1111/j.1699-0463.1996.tb04906.x.

[25] M. Rengarajan, A. Hayer, J.A. Theriot, Endothelial cells use a Formin-dependent phagocytosis-like process to internalize the bacterium listeria monocytogenes, PLoS Pathog. 12 (2016), e1005603, https://doi.org/10.1371/journal.ppat.1005603.

[26] J. Thomas, D. Jones, L. Moldovan, M. Anghelina, K.J. Gooch, N.I. Moldovan, Labeling of endothelial cells with magnetic microbeads by angiophagy, Biotechnol. Lett. 40 (2018) 1189–1200, https://doi.org/10.1007/s10529-018-2581-9.

[27] S.A.G. Langeveld, B. Meijlink, K. Kooiman, Phospholipid-coated targeted microbubbles for ultrasound molecular imaging and therapy, Curr. Opin. Chem. Biol. 63 (2021) 171–179, https://doi.org/10.1016/j.cbpa.2021.04.013.

[28] S.A.G. Langeveld, C. Schwieger, I. Beekers, J. Blaffert, T. van Rooij, A. Blume, K. Kooiman, Ligand distribution and lipid phase behavior in phospholipid-coated microbubbles and monolayers, Langmuir. 36 (2020) 3221–3233, https://doi.org/10.1021/acs.langmuir.9b03912.

[29] A.L. Klibanov, P.T. Rasche, M.S. Hughes, J.K. Wojdyla, K.P. Galen, J.H. Wible, G. H. Brandenburger, Detection of individual microbubbles of ultrasound contrast agents: imaging of free-floating and targeted bubbles, Investig. Radiol. 39 (2004) 187–195, https://doi.org/10.1097/01.rli.0000115926.96796.75.

[30] J.R. Lindner, J. Song, J. Christiansen, A.L. Klibanov, F. Xu, K. Ley, Ultrasound assessment of inflammation and renal tissue injury with microbubbles targeted to P-selectin, Circulation. 104 (2001) 2107–2112, https://doi.org/10.1161/hc4201.097061.

[31] K. Kooiman, M. Foppen-Harteveld, A.F.W. van der Steen, N. de Jong, Sonoporation of endothelial cells by vibrating targeted microbubbles, J. Control. Release 154 (2011) 35–41, https://doi.org/10.1016/j.jconrel.2011.04.008.

[32] I. Beekers, T. van Rooij, A.F.W. van der Steen, N. de Jong, M.D. Verweij, K. Kooiman, Acoustic characterization of the CLINIcell for ultrasound contrast agent studies, IEEE Trans. Ultrason. Ferroelectr. Freq. Control 66 (2019) 244–246, https://doi.org/10.1109/TUFFC.2018.2881724.

[33] C.T. Chin, C. Lancée, J. Borsboom, F. Mastik, M.E. Frijlink, N. de Jong, M. Versluis, D. Lohse, Brandaris 128: a digital 25 million frames per second camera with 128 highly sensitive frames, Rev. Sci. Instrum. 74 (2003) 5026–5034, https://doi.org/10.1063/1.1626013.

[34] I. Beekers, K.R. Lattwein, J.J.P. Kouijzer, S.A.G. Langeveld, M. Vegter, R. Beurskens, F. Mastik, R. Verduyn Lunel, E. Verver, A.F.W. van der Steen, N. de Jong, K. Kooiman, Combined Confocal Microscope and Brandaris 128 Ultra-High-Speed Camera, Ultrasound Med. Biol. 45 (2019) 2575–2582, https://doi.org/10.1016/j.ultrasmedbio.2019.06.004.

[35] X. Chen, J. Wang, M. Versluis, N. de Jong, F.S. Villanueva, Ultra-fast bright field and fluorescence imaging of the dynamics of micrometer-sized objects, Rev. Sci. Instrum. 84 (2013), 063701, https://doi.org/10.1063/1.4809168.

[36] K.W. Dunn, E. Wang, Optical aberrations and objective choice in multicolor confocal microscopy, Biotechniques. 28 (2000) 542–550, https://doi.org/10.2144/00283rr03.

[37] L. Schermelleh, R. Heintzmann, H. Leonhardt, A guide to super-resolution fluorescence microscopy, J. Cell Biol. 190 (2010) 165–175, https://doi.org/10.1083/jcb.201002018.

[38] S.M. van der Meer, B. Dollet, M.M. Voormolen, C.T. Chin, A. Bouakaz, N. de Jong, M. Versluis, D. Lohse, Microbubble spectroscopy of ultrasound contrast agents, J. Acoust. Soc. Am. 121 (2007) 648–656, https://doi.org/10.1121/1.2390673.

[39] Z. Fan, H. Liu, M. Mayer, C.X. Deng, Spatiotemporally controlled single cell sonoporation, Proc. Natl. Acad. Sci. 109 (2012) 16486–16491, https://doi.org/10.1073/pnas.1208198109.

[40] T. van Rooij, I. Skachkov, I. Beekers, K.R. Lattwein, J.D. Voorneveld, T.J. A. Kokhuis, D. Bera, Y. Luan, A.F.W. van der Steen, N. de Jong, K. Kooiman, Viability of endothelial cells after ultrasound-mediated sonoporation: influence of targeting, oscillation, and displacement of microbubbles, J. Control. Release 238 (2016) 197–211, https://doi.org/10.1016/j.jconrel.2016.07.037.

[41] R.E. Serda, S. Ferrati, B. Godin, E. Tasciotti, X. Liu, M. Ferrari, Mitotic trafficking of silicon microparticles, Nanoscale. 1 (2009) 250–259, https://doi.org/10.1039/b9nr00138g.

[42] J.R. Lindner, P.A. Dayton, M.P. Coggins, K. Ley, J. Song, K. Ferrara, S. Kaul, Noninvasive imaging of inflammation by ultrasound detection of phagocytosed microbubbles, Circulation. 102 (2000) 531–538, https://doi.org/10.1161/01.CIR.102.5.531.

[43] M. Ahmed, B. Cerroni, A. Razuvaev, J. Härmark, G. Paradossi, K. Caidahl, B. Gustafsson, Cellular uptake of plain and SPION-modified microbubbles for potential use in molecular imaging, Cell. Mol. Bioeng. 10 (2017) 537–548, https://doi.org/10.1007/s12195-017-0504-9.

[44] A.D. Terrisse, N. Puech, S. Allart, P. Gourdy, J.M. Xuereb, B. Payrastre, P. Sié, Internalization of microparticles by endothelial cells promotes platelet/endothelial cell interaction under flow, J. Thromb. Haemost. 8 (2010) 2810–2819, https://doi.org/10.1111/j.1538-7836.2010.04088.x.

[45] C.J. Treutiger, A. Heddini, V. Fernandez, W.A. Muller, M. Wahlgren, PECAM-1/CD31, an endothelial receptor for binding plasmodium falciparum- infected erythrocytes, Nat. Med. 3 (1997) 1405–1408, https://doi.org/10.1038/nm1297-1405.

[46] S. Muro, R. Wiewrodt, A. Thomas, L. Koniaris, S.M. Albelda, V.R. Muzykantov, M. Koval, A novel endocytic pathway induced by clustering endothelial ICAM-1 or PECAM-1, J. Cell Sci. 116 (2003) 1599–1609, https://doi.org/10.1242/jcs.00367.

[47] P.A. Dayton, J.E. Chomas, A.F.H. Lum, J.S. Allen, J.R. Lindner, S.I. Simon, K. W. Ferrara, Optical and acoustical dynamics of microbubble contrast agents inside neutrophils, Biophys. J. 80 (2001) 1547–1556, https://doi.org/10.1016/S0006-3495(01)76127-9.

[48] D.C. Walker, A. MacKenzie, S. Hosford, The structure of the Tricellular region of endothelial tight junctions of pulmonary capillaries analyzed by freeze-fracture, Microvasc. Res. 48 (1994) 259–281, https://doi.org/10.1006/mvre.1994.1054.

[49] A.R. Burns, D.C. Walker, E.S. Brown, L.T. Thurmon, R.A. Bowden, C.R. Keese, S. I. Simon, M.L. Entman, C.W. Smith, Neutrophil transendothelial migration is independent of tight junctions and occurs preferentially at tricellular corners, J. Immunol. 159 (1997) 2893–2903.

[50] E.E. Konofagou, Optimization of the ultrasound-induced blood-brain barrier opening, Theranostics. 2 (2012) 1223–1237, https://doi.org/10.7150/thno.5576.

[51] J. Park, Z. Fan, C.X. Deng, Effects of shear stress cultivation on cell membrane disruption and intracellular calcium concentration in sonoporation of endothelial cells, J. Biomech. 44 (2011) 164–169, https://doi.org/10.1016/j.jbiomech.2010.09.003.

[52] H.J. Vos, B. Dollet, J.G. Bosch, M. Versluis, N. de Jong, Nonspherical vibrations of microbubbles in contact with a wall—a pilot study at low mechanical index, Ultrasound Med. Biol. 34 (2008) 685–688, https://doi.org/10.1016/j.ultrasmedbio.2007.10.001.

[53] M. Overvelde, V. Garbin, B. Dollet, N. de Jong, D. Lohse, M. Versluis, Dynamics of coated microbubbles adherent to a wall, Ultrasound Med. Biol. 37 (2011) 1500–1508, https://doi.org/10.1016/j.ultrasmedbio.2011.05.025.

[54] B.L. Helfield, B.Y.C. Leung, D.E. Goertz, The effect of boundary proximity on the response of individual ultrasound contrast agent microbubbles, Phys. Med. Biol. 59 (2014) 1721–1745, https://doi.org/10.1088/0031-9155/59/7/1721.

[55] F.E. Shamout, A.N. Pouliopoulos, P. Lee, S. Bonaccorsi, L. Towhidi, R. Krams, J. J. Choi, Enhancement of non-invasive trans-membrane drug delivery using ultrasound and microbubbles during physiologically relevant flow, Ultrasound Med. Biol. 41 (2015) 2435–2448, https://doi.org/10.1016/j.ultrasmedbio.2015.05.003.

[56] E.K. Juang, I. De Cock, C. Keravnou, M.K. Gallagher, S.B. Keller, Y. Zheng, M. Averkiou, Engineered 3D microvascular networks for the study of ultrasound-microbubble-mediated drug delivery, Langmuir. 35 (2019) 10128–10138, https://doi.org/10.1021/acs.langmuir.8b03288.

[57] D. Qin, L. Zhang, N. Chang, P. Ni, Y. Zong, A. Bouakaz, M. Wan, Y. Feng, In situ observation of single cell response to acoustic droplet vaporization: membrane deformation, permeabilization, and blebbing, Ultrason. Sonochem. 47 (2018) 141–150, https://doi.org/10.1016/j.ultsonch.2018.02.004.

[58] M. Edidin, A rapid, quantitative fluorescence assay for cell damage by cytotoxic antibodies, J. Immunol. 104 (1970) 1303–1306. http://www.jimmunol.org/content/104/5/1303.abstract.

[59] G. Lajoinie, I. De Cock, C.C. Coussios, I. Lentacker, S. Le Gac, E. Stride, M. Versluis, In vitro methods to study bubble-cell interactions: fundamentals and therapeutic applications, Biomicrofluidics. 10 (2016), https://doi.org/10.1063/1.4940429.

[60] C. Elfgang, R. Eckert, H. Lichtenberg-Fraté, A. Butterweck, O. Traub, R.A. Klein, D. F. Hülser, K. Willecke, Specific permeability and selective formation of gap junction channels in connexin-transfected HeLa cells, J. Cell Biol. 129 (1995) 805–817, https://doi.org/10.1083/jcb.129.3.805.

[61] H.M. Shapiro, Practical Flow Cytometry, Wiley, 2003, https://doi.org/10.1002/0471722731.

[62] G. Paganelli, C. Belloni, P. Magnani, F. Zito, A. Pasini, I. Sassi, M. Meroni, M. Mariani, M. Vignali, A.G. Siccardi, F. Fazio, Two-step tumour targetting in ovarian cancer patients using biotinylated monoclonal antibodies and radioactive streptavidin, Eur. J. Nucl. Med. 19 (1992) 322–329, https://doi.org/10.1007/BF00177053.

[63] H.B. Breitz, P.L. Weiden, P.L. Beaumier, D.B. Axworthy, C. Seiler, F.M. Su, S. Graves, K. Bryan, J.M. Reno, Clinical optimization of pretargeted radioimmunotherapy with antibody-streptavidin conjugate and 90Y-DOTA-biotin, J. Nucl. Med. 41 (2000) 131–140.

[64] K. Otani, H. Nishimura, A. Kamiya, M. Harada-Shiba, Simplified preparation of αvβ3 integrin-targeted microbubbles based on a clinically available ultrasound contrast agent: validation in a tumor-bearing mouse model, Ultrasound Med. Biol. 44 (2018) 1063–1073, https://doi.org/10.1016/j.ultrasmedbio.2018.01.017.

[65] S. Unnikrishnan, Z. Du, G.B. Diakova, A.L. Klibanov, Formation of microbubbles for targeted ultrasound contrast imaging: practical translation considerations, Langmuir. 35 (2019) 10034–10041, https://doi.org/10.1021/acs.langmuir.8b03551.

[66] J. Zhang, S. Wang, Z. Deng, L. Li, G. Tan, X. Liu, H. Zheng, F. Yan, Ultrasound-triggered drug delivery for breast tumor therapy through iRGD-targeted paclitaxel-loaded liposome-microbubble complexes, J. Biomed. Nanotechnol. 14 (2018) 1384–1395, https://doi.org/10.1166/jbn.2018.2594.

[67] H. Leong-Poi, J. Christiansen, A.L. Klibanov, S. Kaul, J.R. Lindner, Noninvasive assessment of angiogenesis by ultrasound and microbubbles targeted to αv-integrins, Circulation. 107 (2003) 455–460, https://doi.org/10.1161/01.CIR.0000044916.05919.8B.

[68] V. Daeichin, K. Kooiman, I. Skachkov, J.G. Bosch, T.L. Theelen, K. Steiger, A. Needles, B.J. Janssen, M.J.A.P. Daemen, A.F.W. van der Steen, N. de Jong, J.

C. Sluimer, Quantification of endothelial αvβ3 expression with high-frequency ultrasound and targeted microbubbles: in vitro and in vivo studies, Ultrasound Med. Biol. 42 (2016) 2283–2293, https://doi.org/10.1016/j.ultrasmedbio.2016.05.005.